SIMULATION OF A DUAL ARM FISSION FRAGMENT SPECTROMETER

by

William P. Moore

A thesis submitted to the Faculty and the Board of Trustees of the Colorado School of Mines in partial fulfillment of the requirements for the degree of Master of Science (Nuclear Engineering).

Golden, Colorado

Date 3/30/11

Signed:
William P. Moore

Signed:
Dr. Uwe Greife
Professor

Golden, Colorado

Date 3/31/11

Signed:
Dr. Jeffrey King
Assistant Professor and Interim Director
Nuclear Science and Engineering Program

ABSTRACT

The Colorado School of Mines (CSM) and Los Alamos National Laboratory (LANL) are establishing a basic fission fragment research program to produce experimental data that can be used to supplement and verify advances in theoretical fission models. A state of the art dual arm, time of flight and energy (TOF-E) detector system is being designed and optimized for this purpose, with the goal of achieving the smallest mass resolution possible while maintaining as large of a solid angle as possible. A Monte Carlo simulation is needed to predict the achivable energy, angle, and timing resolution of the design. Geant4, a physics toolkit for simulating the passage of particles through matter, was used to optimize the detector, and predict the achievable mass resolution. Simulations were conducted changing arm length, source thickness, source diameter, foil thickness, and detector type. The dominant contribution to the mass resolution came from the energy resolution of the silicon detectors, and the second largest contribution was the timing resolution of the microchannel plate (MCP) detectors. For maximum solid angle, the shortest arm length (20 cm) and largest diameter source (20 mm) should be used, and position-sensitivity is necessary in the silicon detector to obtain optimal mass resolution. The source thickness was found to have no effect on the mass resolution, therefore a source thickness on the order of 200 μg/cm^2 is possible. For total kinetic energy measurements the energy loss of fission fragments in the source should be minimized by using the thinnest source possible. The thickness of the secondary electron producing carbon foil was found to contribute to the detector timing resolution making the thinnest possible foil ideal. The use of gas filled ionization chambers can provide improved energy resolution over silicon detectors making them a more logical choice based on these results. Ionization chambers lack position sensitivity requiring the use of position sensitive MCP detectors.

TABLE OF CONTENTS

LIST OF FIGURES

LIST OF TABLES

ACKNOWLEDGEMENTS

I would first like to thank Dr. Uwe Greife for his support, guidance and for giving me the opportunity to do this research. This thesis was made possible through the support of my colleagues, family and friends. I would also like to thank Luke Snyder for his continued guidance along the way. Thanks to Jon Toebbe, Luke Erikson, and Duane Smalley for the C++ and ROOT help they provided me. Finally, I would like to acknowledge and thank Dr. Fredrik Tovesson (LANL) for discussions on my work.

CHAPTER 1

INTRODUCTION

Current models of fission are generally capable of paramaterizing existing data, but have very little predictive power. Advances in fission cross section as well as fission fragment yield measurements are needed to constrain theoretical descriptions of fission. In this chapter, I will present a brief summary on the progression of various fission models. I will present the motivation behind this thesis, and describe the scope of my work.

1.1 Background

Detailed knowledge of the nucleon-nucleon interaction constitutes a precursor to an understanding of the interaction between free nucleons and nuclei. The nucleon-nucleon interaction can be deduced from the analysis of scattering experiments(1). This interaction is well known, however it fails to provide a detailed description of the structure of an atomic nucleus. In fact, certain nuclear characteristics cannot be described with precision from knowledge of the nucleon-nucleon interaction alone, and this is a general characteristic of many body systems(2). Rather than focus on fine details such as the individual forces between particles, simplified models were developed to account for the overall behavior of the system.

Models that describe the nucleus can be classified into two classes: Independent-Particle models (IPM) and Strong-Interaction models (SIM)(2). Models that describe characteristics of the nucleus as a whole using the behavior of individual particles within a nucleus are classified as IPM. Models that reflect the strong, short-range nature of the internucleonic force in which nucleons are taken to be strongly coupled to one another are classified as SIM. The Fermi-gas model, Potential-well model, Optical model, and Shell model are a few examples belonging to the IPM class, while the Liquid-drop model, Compound-nucleus model, and Unified model are some examples that belong to the SIM class.

Every model begins with fundamental properties of internucleonic forces and attempts to render an acceptable systematic account of diverse nuclear properties such as energies, spins, parities, electric and magnetic moments of nuclear states, level densities, binding energies and masses of nuclides, pairing energies, the phenomena of fission, resonance capture, isomerism, decay characteristics, and the occurrence of irregularities or discontinuities in the properties listed[3]. Although no single model is able to describe all of these characteristics with precision, it is clear that both types of models have usefulness in the explanation of certain nuclear properties. An example of this is used for the description and prediction of nuclear masses and reaction Q-values.

The *semiempirical mass formula* was derived from different varieties of nuclear models such as the Liquid-drop model and the Shell model, and can be seen in Equation 1.1[4], where A is the mass number, Z is the number of protons, N is the number of neutrons, m is the mass, and $B(A, Z)$ is the binding energy defined in Equation 1.2[4]. The formula was originally developed using the Liquid-drop model, and the theory was fairly successful in describing the binding energy of stable nuclei.

$$M(Z, A) = Zm(^1H) + Nm_n - \frac{B(Z, A)}{c^2} \tag{1.1}$$

$$B(Z, A) = a_v A - a_s A^{2/3} - a_c Z(Z-1)A^{-1/3} - a_{sym}\frac{(A-2Z)^2}{A} + \delta \tag{1.2}$$

The first term in Equation 1.2 accounts for the *volume* energy, the second term is the *surface* energy, the third term is the *Coulomb* energy, the fourth term is the *asymmetry* term, and the last term is the *pairing* term. The first three terms appear in the calculation of the energy of a charged liquid droplet, thus result from the Liquid-drop model. The last two terms in Equation 1.2 arose from the application of the Shell model. Their inclusion approximated better the periodic discontinuities in the separation energy corresponding to the filling of closed nucleonic shell structures (the so called "magic numbers")[5]. The net result was improving the agreement between the *semiempirical mass formula* and experimental data on the binding energy[6].

The *semiempirical mass formula* is a perfect example of how different models can be used simultaneously to understand the systematic behavior of a nuclear property, in this case the binding energy, provided there is experimental data available for comparison. The importance in the *semiempirical mass formula* is the application of combining nuclear models to describe behavior of a property; the formula does not work well in the prediction of any new or exotic phenomena of nuclear physics[7].

In our current understanding of the fission process, the evolution from the initial compound nucleus to two distinct fission fragments occurs gradually as a result of dissipative multidimensional deformation of the nuclear shape[8]. Since the development of the *multi-modal random neck-rupture model* of Brosa *et al.*[9] in 1983, the theoretical description of fission has significantly improved[10]. The model presented by Vladuca *et al.* presents a good example of the evolution of the multi-modal approach where, for the first time, the mode separated fission cross sections were calculated in the incident neutron energy range of 0.01 to 5.5 MeV, giving good agreement with the experimental fission cross-section data[11].

This description of the fission process is capable of parameterizing existing data, however it has very little predictive capability[12], and fails to accurately describe nuclear fission processes outside the valley of stability on the chart of nuclides. On the neutron rich side of the valley of stability, the fission fragment distributions are expected to change significantly with isotope[13].

1.2 Motivation

Traditional treatments of fission[14] describe integral fission properties, e.g. the average energy release, and the average differential neutron yield. Currently, due to the amount of practical applications of the fission process, more exclusive quantities such as fluctuations in neutron multiplicity are of high interest. This has created a need for the development of fission models that include treatment of fluctuations and correlations of certain observables (e.g. neutron multiplicity)[8].

Advances in fission cross section and fission fragment yield measurements are needed to constrain theoretical descriptions (e.g.[12,15]). A recent workshop entitled "Nuclear Physics and Related Computational Science R&D for Advanced Fuel Cycles"[16] specifically identified the need for new fission cross section measurements, and identified the lack of data in the area of fission fragment yields and their kinetic energies. Precision cross section data (with an accuracy of 1-2%) performed systematically over a large range of incident neutron energies and fissioning nuclides are necessary to improve fission models as well as for high-accuracy simulations of:

- Nuclear criticality
- Transmutation rates
- Effects of radiation damage and heating on fresh/spent fuel
- Material accounting and identification in fresh/spent fuel

Conventional and fast reactors require a neutron energy range coverage from thermal energies to beyond 10 MeV, as can be seen in Figure 1.1.

In 2005, Lemaire *et al.*[18] presented a Monte Carlo simulation of the neutron emission and statistical decay of fission fragments from thermal fission of ^{235}U and from spontaneous fission of ^{252}Cf. The work demonstrates how experimental data, combined with physics models on fission and neutron emission, can be used to develop

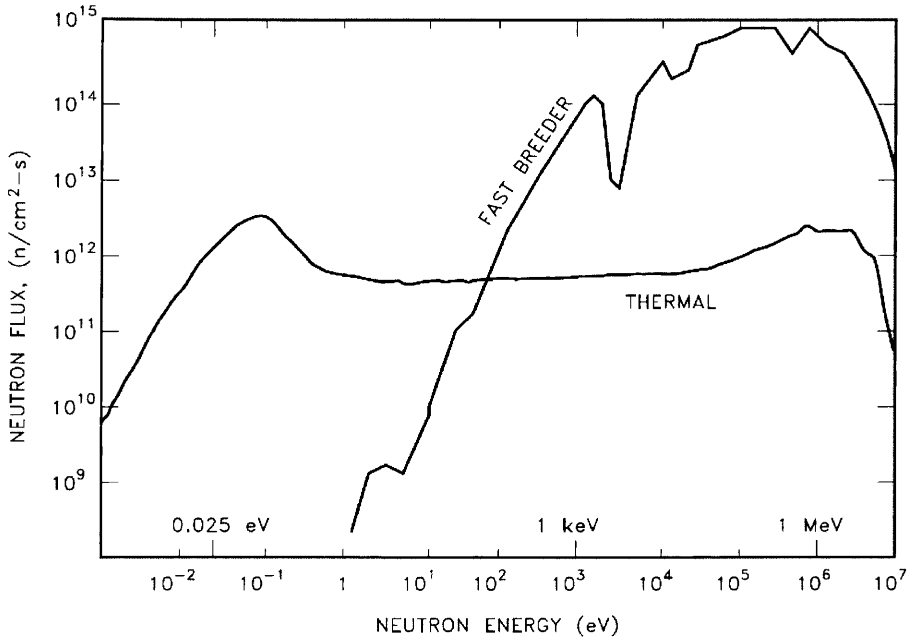

Figure 1.1: Neutron energy spectra for thermal and fast breeder reactors[17].

fission event simulations which can predict the neutron spectrum and improve the underlying physics models[8].

Fission fragment identification and total kinetic energy (TKE) measurement of each fission event can be performed using a dual arm spectrometer (DAS) based on time-of-flight (TOF) and rest energy (E) measurement. It is the purpose of the research presented in this thesis to simulate a starting point for a DAS design, perform several proof of principle tests of possible improvements on previous technologies, and suggest a final design with the goal of obtaining a mass resolution as small as technically feasible.

In the future, based on the final design, the DAS will be constructed at the Colorado School of Mines (CSM), intended for experimentation with multiple fission sources. After initial measurements with a ^{252}Cf spontaneous fission (SF) source, other targets, e.g. ^{235}U, will require a neutron beam to induce fission. The Los Alamos Neutron Science Center (LANSCE) Facility at Los Alamos National Laboratory (LANL) will provide neutron fluxes to perform needed measurements over a wide neutron energy range of interest to the nuclear energy, national nuclear security, and nuclear astrophysics communities. Experiments can then be performed using the DAS with a variety of fissile targets to provide fission fragment yield data necessary to improve theory.

1.3 Task

Proof of principle checks prior to the construction and installation of the DAS can be conducted using Monte Carlo simulation. Geant4[(19)], a physics toolkit which simulates the passage of particles through matter (for the purpose of detector development and experiment interpretation) was used to produce a fission fragment generator that reproduces known fission fragment distributions. A computer model of the initial design of the DAS was constructed and the fission fragment generator was used to test its properties.

In order to guide our design efforts the computer model had the achievable energy, angle, and timing resolution modeling a ^{252}Cf spontaneous fission source, leading to a determination of the overall mass resolution of the DAS. The final design for future construction will be determined based on a compromise between solid angle and mass resolution, optimizing flight time, flight length, foil size, and source size.

CHAPTER 2

PHYSICS OF A DUAL ARM SPECTROMETER

In this chapter, I will present the physics and mathematics relevant to a dual arm spectrometer. A summary of my literature search on previous work led to a preliminary design of the dual arm spectrometer. After selecting a preliminary design, the equations used are presented, as well as any simplifying assumptions made.

2.1 Literature Summary

To fully describe a fission event, a simultaneous measurement of all gammas, neutrons, and fission fragments including detection of energy, direction, and fragment identification is needed. ^{252}Cf undergoes fission spontaneously eliminating the need for a neutron beam to induce fission. Therefore background from the neutron beam does not affect the measurement. This makes ^{252}Cf a good starting point for our investigation.

The basis for comparison of fission fragment experiments with a ^{252}Cf source comes from Henschel et al.[(20)]. In this work, the double energy-single velocity method introduced by Schmitt et al.[(21)] was used with detectors for kinetic energy and time of flight of the surface barrier type. The velocity and kinetic energy measurements on fission fragments of ^{252}Cf were used for mass identification. By assuming the ratio of the final energy to the initial energy is equal to the ratio of the final mass to the initial mass, and applying conservation of linear momentum, the number of neutrons emitted by the fragments was indirectly calculated. However, their calculated fragment masses after prompt neutron emission were found to be too high, due to error in the widely accepted calibration method for silicon surface barrier detectors (SSBD)[(22–24)], which provides an equation relating pulse height to the energy of the fragment as well as a method for determining empirical constants.

The measured energy and time of flight were also used to calculate the mean number of neutrons evaporated off of the fragments as a function of fragment mass. However, the same erroneous trend was produced. The fission fragment mass resolution in this experiment was around 6 amu, mainly limited by the energy calibration of the detectors. Schmidt *et al.*[(25)] used the same calibration method for their SSBDs, with a similar experimental setup, and found the detected kinetic energies to be about 1.9 MeV too high.

A precise measurement including direct neutron detection was performed by Budz-Jorgensen and Knitter[(26)]. A gridded twin ionization chamber was used with an NE213 scintillation detector to measure energy, mass and angular distribution of the fission fragments of the spontaneous fission of ^{252}Cf. A neutron time of flight detector was also used to determine the energies of the emitted neutrons and their angular asymmetries. However, even in a well measured system such as this, theoretical prediction of e.g. the average neutron multiplicity differed significantly from experimental results.

In 1979, Busch *et al.*[(27)] developed an electrostatic mirror, with a carbon foil for secondary electron production, and an electric field to accelerate the secondary electrons toward a multichannel plate detector (MCP). This device served as the start detector for TOF measurements through a magnetic spectrometer. With this setup, the timing resolution was determined to be 150 ps; far better than in any previous experiments.

Measurements of fission fragment distributions using a TOF spectrometer and a MCP for the start signal, and parallel plate avalanche counters (PPACs) for the stop signal were performed by Heil et al.[(28)]. The MCP was used in conjunction with an electrostatic mirror following the methodology presented by Busch *et al.*[(27)], and Della *et al.*[(29)]. The mass resolution for ^{252}Cf fission fragments was about 3 amu, achieved with a timing resolution of about 235 ps. Significant progress was made toward improving the mass resolution using a relatively simple TOF spectrometer.

In 1986, Bakkum *et al.*[30] developed a detection system for heavy residues at low energies consisting of MCP detectors for flight time, an ionization counter as a transmission detector and an array of SSBDs to stop the fragments. They determined the energy straggling of the fragment in the gas of the ionization chamber. A mass resolution of less than 2 amu was achieved.

In 1988, a Dutch group determined that simultaneous measurement of energy and time of flight gives a good post-neutron mass distribution, however accuracy of mass determination for a fragment pair is limited to 1 amu due to sequential neutron emission[31]. This cannot be improved because the neutron emission pattern is fully unknown for a single event. This work also concluded that the most serious limitation on accuracy results from the energy and time calibration.

In the early 1990's, a Swedish group[32] working on medium energy recoil spectrometry used two MCP based timing detectors with electrostatic mirrors, and ion-implanted silicon detectors to determine the TOF and energy[27]. With this setup, they explored in detail the contributions of systematic error to resolution in mass identification in the mass/energy range relevant for fission fragment detection. They determined that error sources lie in:

- Timed flight length
- Energy spread in Carbon foils
- Dead layer of silicon detector
- Timing resolution of MCP detector pair
- Energy resolution of silicon detector (including the so-called pulse height defect)

The uncertainty in timed flight length originates from deformation of the carbon foils, as well as from length variation within the target or detector area. The error due to energy spread in the carbon foils is a result of energy straggling of the fragment in the carbon foil, as well as from density and thickness fluctuations in the carbon foil.

Whitlow et al.[32] identified the energy resolution and pulse height defect (PHD) of the detector, as the dominant source of error in the mass resolution. The PHD is explained in detail later, in Section 3.1.4. With a timing resolution of 170 ps, the mass resolution achieved was less than 3. Based on this approach, using MCP detectors and electrostatics mirrors to measure the TOF, SSBDs to measure energy, and careful treatment of the SSBD PHD and energy calibration[33–37], mass resolution values of 2 amu or better are expected.

The TOF/energy detector telescope method has recently been implemented at the CELSIUS storage ring in Uppsala, for the detection of slow heavy reaction products[38]. Silicon p-i-n diode detectors were used with MCPs to detect energy and TOF respectively. A detailed comparison of silicon p-i-n diode detectors with SSBDs is presented by Gujrathi *et al.*[39], and it was concluded that p-i-n diode detectors can successfully be used in charged-particle detection applications. Their study also determined the energy calibration and PHD correction of the detector as the most crucial point in the mass-energy reconstruction procedure.

2.2 Preliminary Design of the DAS

The initial design of each arm of the ToF-E spectrometer consists of two electrostatic mirrors (see Section 3.1.1) guiding secondary electrons into MCP detectors for the start and stop time signals, with either an SSBD, or a double sided silicon strip detector (DSSSD) to detect the energy of the fission fragment. The preliminary design with DSSSDs can be seen in Figure 2.1.

The Geant4 computer simulation here investigated the effects of changing the arm length, source size/thickness, foil size/thickness, and detector type (changing between a SSBD and a DSSSD), on the overall mass resolution.

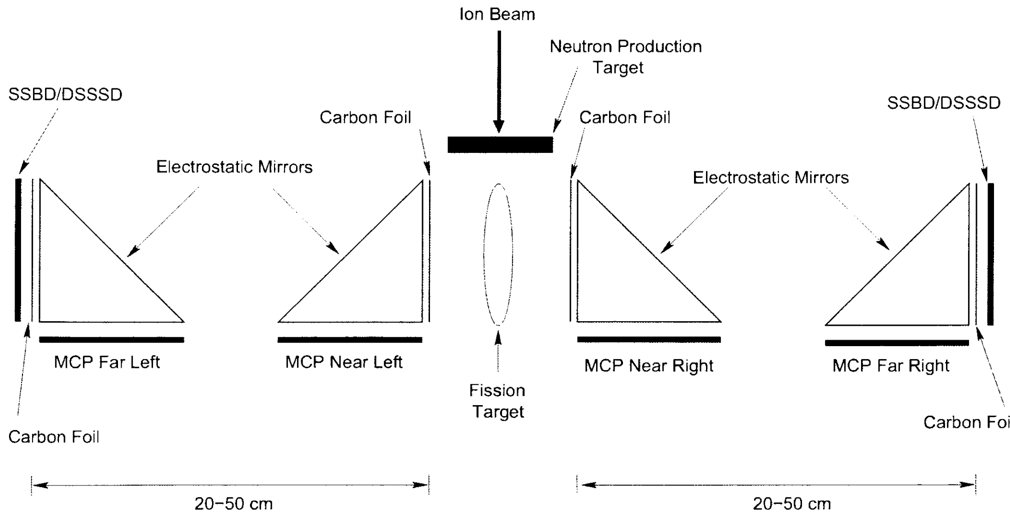

Figure 2.1: Preliminary design of a dual arm spectrometer.

2.3 Mass Calculation

Following the classical description (possible for kinetic energies on the order of 1 MeV/amu) of the time-of-flight method, the mass and energy of the particle are determined by a simultaneous measurement of velocity, v, and total kinetic energy, E[40]. The mass, m, is given by Equation 2.1, where t and l are the flight time and flight path, respectively.

$$m = \frac{2E}{v^2} = \frac{2Et^2}{l^2} \tag{2.1}$$

The mass resolution, $\Delta A/A$, is given by Equation 2.2[41], where ΔE, Δt and Δl are the uncertainties in energy, flight time and flight path, respectively.

$$\frac{\Delta A}{A} = \left[\left(\frac{\Delta E}{E}\right)^2 + \left(2\frac{\Delta t}{t}\right)^2 + \left(2\frac{\Delta l}{l}\right)^2\right]^{1/2} \tag{2.2}$$

As a fragment travels through the arm of the DAS, it has an initial velocity, v_1. Once the fragment collides with the carbon foil in the first electrostatic mirror, it loses energy reducing its velocity, v_2. The fragment will lose more energy after collision with the foil in the second electrostatic mirror, and will travel at a third velocity,

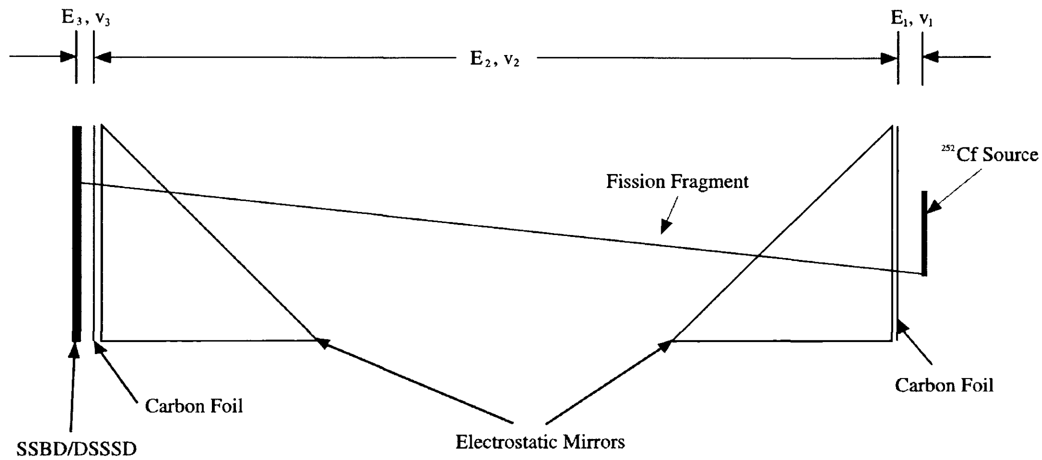

Figure 2.2: Change in velocity and energy of a fission fragment traveling through an arm of a DAS.

v_3. Each velocity has a corresponding energy. The energy of the fragment after exiting the source, E_1, corresponds to v_1; the energy lost in the first foil is subtracted from the initial energy leading to E_2, corresponding to v_2; the energy lost in both foils subtracted from the initial energy results in E_3, corresponding to v_3. A visual representation of this can be seen in Figure 2.2.

Although the fragment loses energy in two foils, one per electrostatic mirror, only a correction factor for the second foil is necessary in the mass calculation. This is because the measured time of flight of the particle corresponds to v_2 in Figure 2.2, and thus v_2 and E_2 must be used in the mass calculation. This means also that for the purpose of mass identification, the thickness of the ^{252}Cf source does not matter. The energy the fragment loses in the first carbon foil is not relevant for the mass identification. However, foil thickness is still important. It is shown in Section 4.2.4 that the thickness of the foil is important to achieve optimal timing resolution.

The fission fragment will experience energy loss and straggling in a carbon foil, and this will contribute to the uncertainty in the measured energy. For the purpose of calculating the mass, E_1 is irrelevant because there is no way to determine v_1. Actually, v_2 is the only velocity we can directly determine, by taking the start and stop time signals from the MCPs. The energy detected by the silicon detector is E_3, which is equal to E_2 minus the energy deposited in the second carbon foil.

Since we have no way of detecting the energy lost by the fission fragments in the second foil, some kind of correction factor has to be added to E_3, or every mass calculated will be underestimated. Applying a correction factor to the mass equation will not affect the statistical uncertainty. In other words, the correction factor will cause the mean of the histogram to shift to the right, to the proper mass, but it will not alter the FWHM or shape of the histogram. It might however introduce a systematic error.

During experimentation, it will be possible to estimate the energy lost by the fission fragment in the foil using the stopping power program called The Stopping and Range of Ions in Matter (SRIM) based on tabulation of experimental data and extrapolation. Geant4 has the capability of computing the energy lost by the fission fragment as it passes through the foil, so a similar approximation to SRIM was achieved by programming the simulation to store the energy lost by each fragment in the second foil. The mean value for the energy lost by the fission fragment in the foil, $E_{f,ave}$, was used as the correction factor in the mass calculation, seen in Equation 2.3.

$$m = 2(E + E_{f,ave})\frac{t^2}{l^2} \tag{2.3}$$

Also, if needed in experimentation, Knyazheva *et al.*[(42)] presented a detailed study on the energy loss of ^{252}Cf fission fragments in thin foils. An example histogram of the energy deposited in the foil can be seen in Figure 2.3.

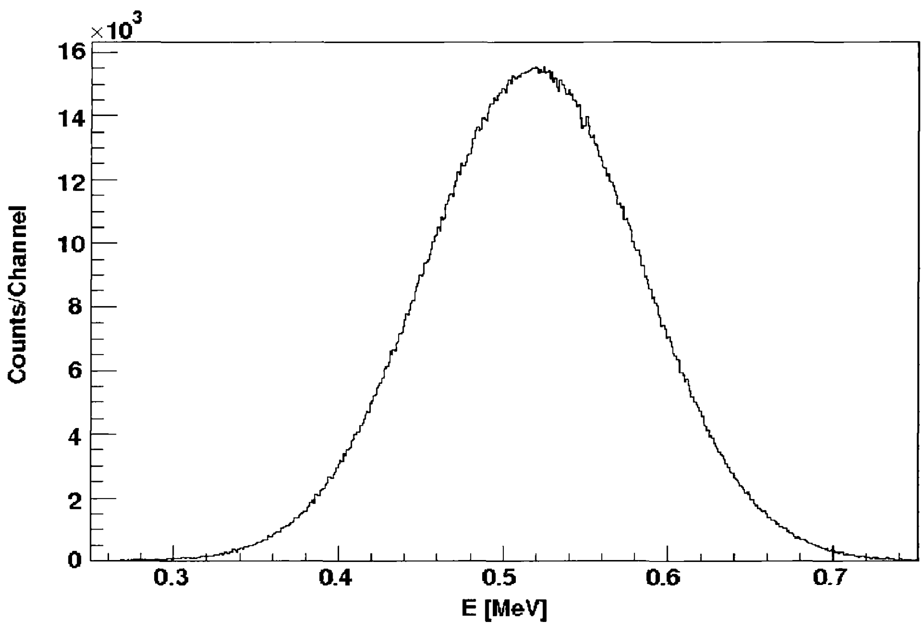

Figure 2.3: Energy deposited in the carbon foil by a fission fragmentwith A = 84.

CHAPTER 3

GEANT4 SIMULATION

In this chapter, details and parameters of my simulation are described. A description of each component in the design is presented, as well as how it was simulated in Geant4. A description of how the ^{252}Cf particle generator was simulated is also presented, followed by a description of the fission fragment source.

3.1 Spectrometer Components

Each arm of the simulated spectrometer has two electrostatic mirrors, two MCPs, and a silicon detector (SSB or DSSSD). The setup of the dual arm spectrometer can be seen in Figure 2.1.

For the purpose of this simulation, the fission fragment source will be ^{252}Cf, which undergoes fission spontaneously, eliminating the need for the neutron production seen in Figure 2.1. However, eventually the dual arm spectrometer will be used with other fission targets, which will require a neutron beam to induce fission.

After fission, if the fragment is emitted into the solid angle subtended by the DAS, the fragment will travel into the first electrostatic mirror, where it will collide with a thin carbon foil, producing secondary electrons. The electrons will be accelerated towards the first MCP, which will register a charge pulse when impacted (start signal). The fragment will continue to the second electrostatic mirror where the process will repeat itself to get the stop signal, from which the time of flight can be calculated.

The electric fields in the electrostatic mirrors are not strong enough to have a measurable impact on the momentum of the fragment. After the fragment has passed through the second electrostatic mirror, it will collide with the silicon detector, depositing its remaining energy.

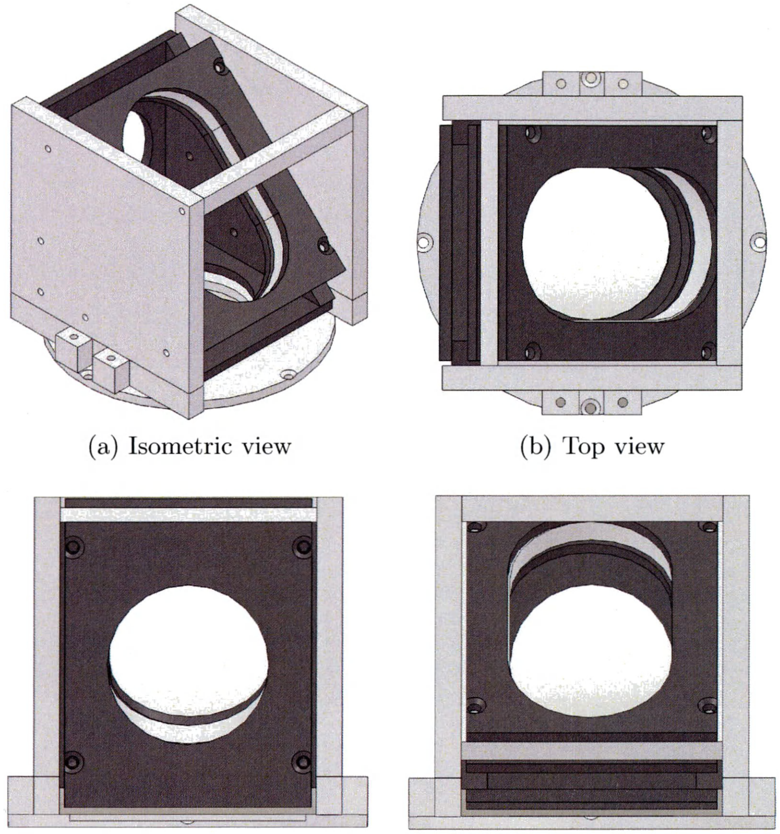

(a) Isometric view
(b) Top view
(c) Left view
(d) Right view

Figure 3.1: An electrostatic mirror.

3.1.1 Electrostatic Mirror

Several views of the existing electrostatic mirror can be seen in Figure 3.1, where aluminum components are represented with dark grey, and plastic components are represented with off-white. The entrance and exit plates have 2.0 cm radius circular hole cutouts in the center. The two entrance plates have a thin carbon foil mounted between them for secondary electron production. The exit plate has an MCP mounted just outside, and the hole cutout in the exit plate allows the secondary electrons produced in the carbon foil to pass through and impact the MCP. A diagram of the layout of an electrostatic mirror can be seen in Figure 3.2. Some of the geometric limitations of the existing setup were not used in the geometry of the simulation, e.g.

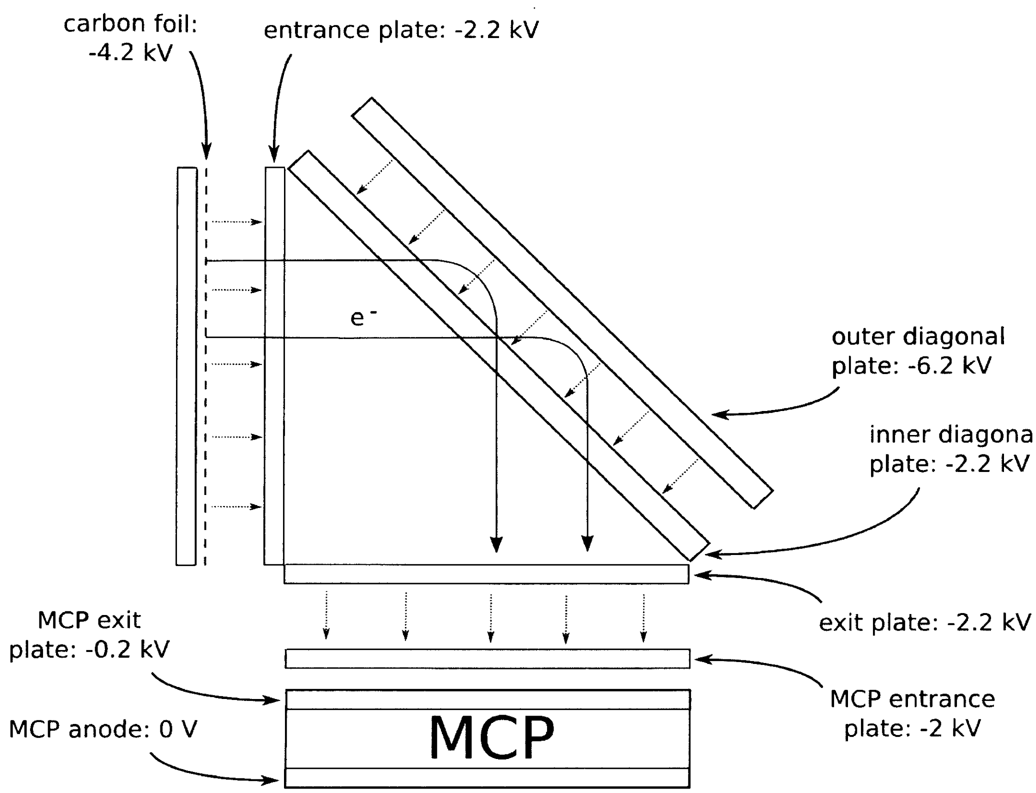

Figure 3.2: Layout of an electrostatic mirror (Overhead view).

carbon foil sizes were chosen to allow full illumination of the silicon detectors.

Voltages are applied to the plates as seen in Figure 3.2[27], creating electric fields to accelerate the secondary electrons in the direction of the MCP. To define the electric field in the regions of space where there are holes cutout in the plates, gold coated, tungsten wires (not shown in Figure 3.2) with a diameter of 25 μm, and a 1 mm spacing were attached to each charged plate using conductive epoxy.

The range of fission fragments from ^{252}Cf in aluminum[43] is significantly less than the thickness of the aluminum plates (on the order of 10^{-5} %), therefore fragments that impact the electrostatic mirror are stopped in the aluminum. Similarly, fragments that hit the tungsten wires will also be stopped in the tungsten.

3.1.2 Microchannel Plate Timing Detector

Microchannel plates were originally developed as high resolution electron amplification devices for image intensifiers[44]. A microchannel plate detector (MCP) is made up of glass plates containing pores typically 12 μm in diameter with 15 μm center-to-center spacing. Each glass plate has Nichrome or Inconel deposited on its front and rear surfaces, which provides parallel electrical contact to each channel.

When an incident electron/photon strikes the channel wall, secondary electrons are produced. Both sides of the plate have a voltage applied to them causing the electrons to accelerate down the pore, continuously impacting the channel wall, creating a cascade of electrons in each microchannel plate. An image showing a single microchannel plate is seen in Figure 3.3. Two microchannel plates used in cascade can reach electron multiplication factors of 10^7, and a timing resolution of less than 100 ps.

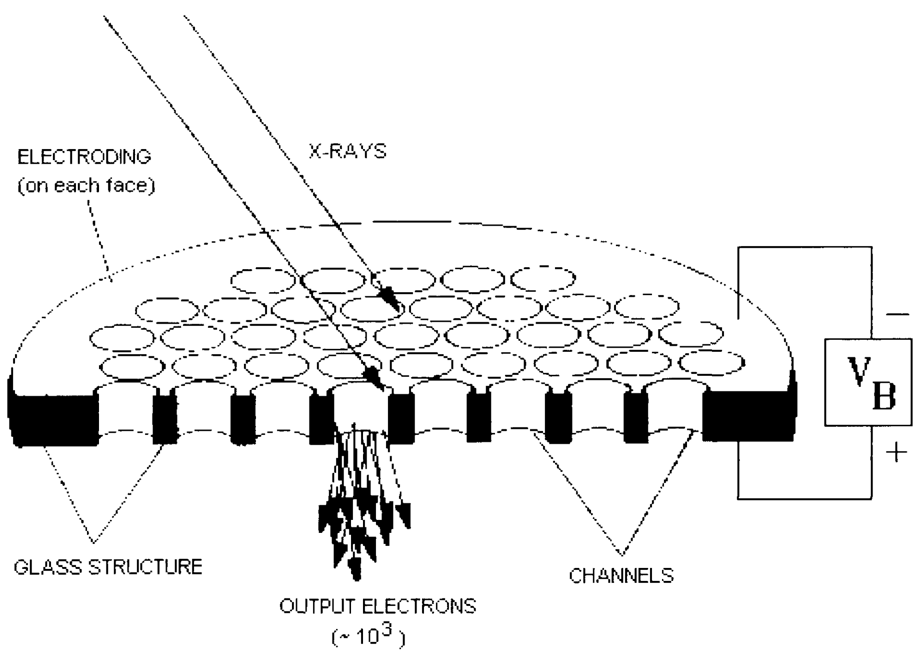

Figure 3.3: A microchannel plate[44].

3.1.3 Simulating the MCP

Modeling the internal processes of the MCP was not required for this simulation. Experimentally, the electrons would enter the MCP, and the MCP would register a charge pulse, used as a timing signal. For the purpose of the simulation, it was sufficient to duplicate this process by modeling the MCP as an aluminum block that stopped and absorbed the electrons, and stored the time of the impact.

The resulting timing resolution of the electrostatic mirror in the simulation was found to be about $\Delta t = 165$ ps, seen in Figure 3.4. This is actually a fairly good approximation of the timing resolution achievable in experimentation, and confirmed the numbers we expect from experiment. In order to avoid long computing times we decided to incorporate a defined timing resolution of actual MCPs.

Instead of taking the timing signal from the instant the electron impacted the MCP, the simulation was programmed to take time signals from the instant the fragment impacts each carbon foil. This has the effect of simulating perfect timing

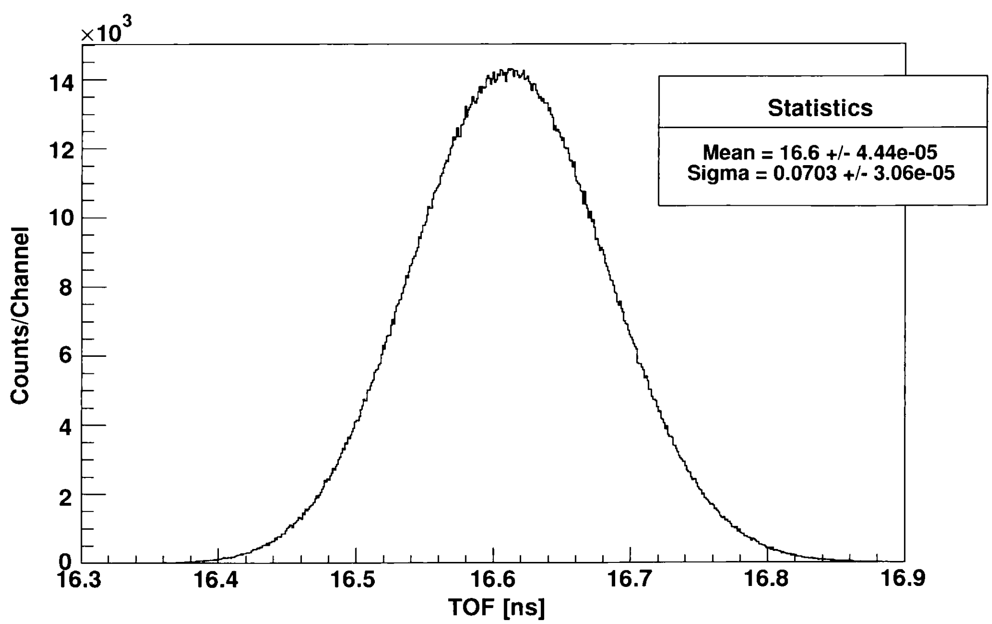

Figure 3.4: Time resolution of simulated MCPs.

resolution, requiring timing resolution to be applied in the post simulation analysis.

With an MCP, a timing resolution of less than 100 ps is achievable[44], but a more realistic starting value is somewhere around twice that. To determine the effect of timing resolution on the mass resolution, the mass resolution was calculated using both 100 and 200 ps resolution values.

3.1.4 Silicon Energy Detector

Surface barrier detectors are composed of p-type and n-type material that form a junction containing a high density of electron traps, or holes. Traditionally, silicon is used as the n-type material, and the p-type material is a gold surface-barrier contact[45]. A p-type crystal could also be used by evaporating aluminum on the surface to form the n-type contact. A depletion region (high density of electron traps) is formed at the junction by applying reverse bias. Today, these p-n junctions are most often produced through implantation of a dopant into the surface of n- or p-type silicon.

Electrons from the incident charged particle will produce electron-hole pairs in the depletion region, which are collected by the electric field generated from applying the reverse bias. The p-type material is generally heavily doped compared to the n-type material causing the depletion region to extend primarily into the n side of the junction. A resultant dead layer is formed by the part of the surface layer that remains outside of the depletion region. Incident charged particles must pass through the dead layer before reaching the depletion region, and the energy lost by the particle as it passes through the dead layer cannot be detected. Thus the dead layer introduces uncertainty in the detected energy of the particle.

The larger the nuclear charge of heavy ions (such as fission fragments), the greater the tendency the ion has to lose energy through nuclear collisions (leading to phonon excitations), not just electronic interactions. However, only energy loss due to electronic interactions in the depletion region is what is registered in the read out of the detectors. There is also a high rate of electron-hole recombination in the plasma tunnel created along the ion track. This eliminates vacancies for electrons, thus reducing the number of electrons in the signal, and increasing the uncertainty in the detected energy of the particle.

The dead layer, the tendency for heavy ions to undergo nuclear interactions, and the high rate of electron-hole recombination all contribute to the uncertainty in the detected energy. These three factors cause the pulse height observed for heavy ions to be significantly less than the pulse height observed for light ions with the same energy. The difference between the true energy of the ion, and the observed energy (determined from an energy calibration) of the ion is known as the pulse height defect (PHD).

The mass resolution is ultimately limited by the energy resolution of the detector, $\Delta E/E$[40]. There have been no systematic, quantitative studies on the energy resolution of SSBDs as a function of mass number and energy for fission fragments using different silicon detectors. However, available data can be approximately reproduced using Equation 3.1[46], where A is the mass number, and ε is the fragment energy expressed in MeV/amu.

$$\frac{\Delta E}{E} = 5 \times 10^{-3} \left(\frac{1 + 0.01A}{\varepsilon^{1/2}} \right) \tag{3.1}$$

The energy of the fragment was calculated using momentum conservation (Equation 3.2), where E is the energy of the fragment in MeV, $E_{sf,Cf}$ is the mean total kinetic energy release from ^{252}Cf (SF), assumed to be 181.25 MeV (see Section 3.2.1), and A_{Cf} is the mass of ^{252}Cf in amu.

$$E = E_{sf,Cf} \frac{A_{Cf} - m}{A_{Cf}} \tag{3.2}$$

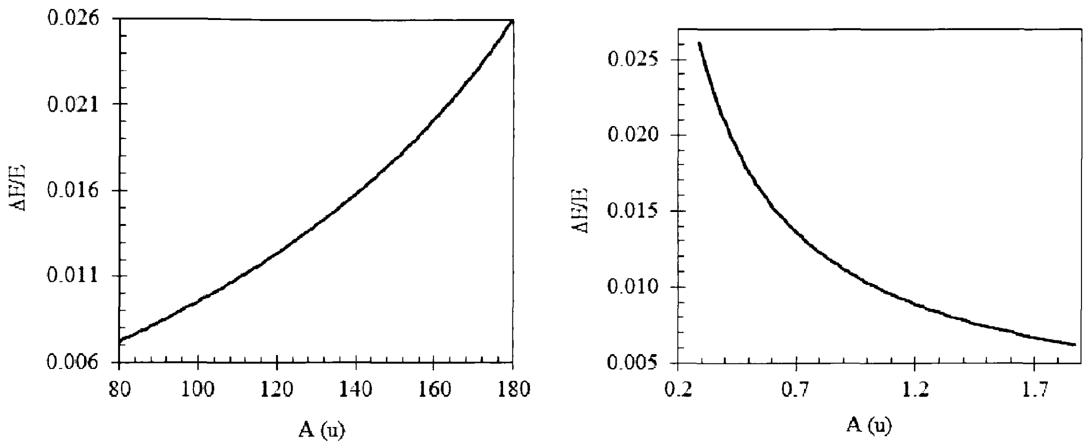

(a) Energy resolution as a function of mass number

(b) Energy resolution as a function of the ratio of energy to mass number

Figure 3.5: Energy resolution of a silicon surface barrier detector.

A plot showing the energy resolution as a function of mass number can be seen in Figure 3.5(a). As mass number increases, the energy carried by the fission fragment decreases. Assuming the absolute uncertainty in energy is constant for every mass value, the relative uncertainty in energy increases as the energy of the fragment decreases. This effect is also displayed in Figure 3.5(b) where it is clear that for larger mass values (with corresponding smaller energies) the relative uncertainty is the greatest.

The first type of detector used in the simulation was a non-segmented SSBD. The silicon block is 5 cm x 5 cm, with a 150 μm thickness. When a fragment collides with the detector, it is stopped in the silicon and deposits its remaining energy. The SSBD does not provide any information regarding the position at which the fragment struck the detector. For this reason, the SSBD gives very poor spatial resolution. There are variations in the fragment's path length (seen in Figure 3.6), and it is impossible to determine the exact path length of the fragment. There is also no way to reconstruct the location of the fragment's origin in the source. This lack of information results in a degradation of the mass resolution.

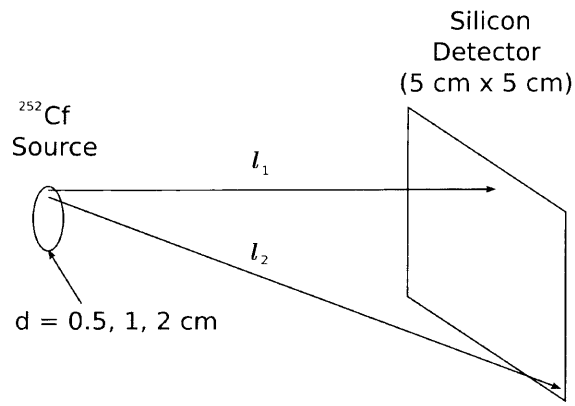

Figure 3.6: Changes in fragment path length.

Just as in a SSBD, as a charged particle is passing through a DSSSD, the particle creates ionization in the bulk of the silicon. Electrons are promoted into the conduction band leaving vacancies, or holes. In the p-type material, electron vacancies are attracted toward the negative charge, and the electrons are attracted towards the back plane of the detector, where aluminum strips are positively charged. When the electron vacancies reach the aluminum contacts, they are collected and induce a measurable charge on the strip readout. A cross-sectional view of a DSSSD can be seen in Figure 3.7.

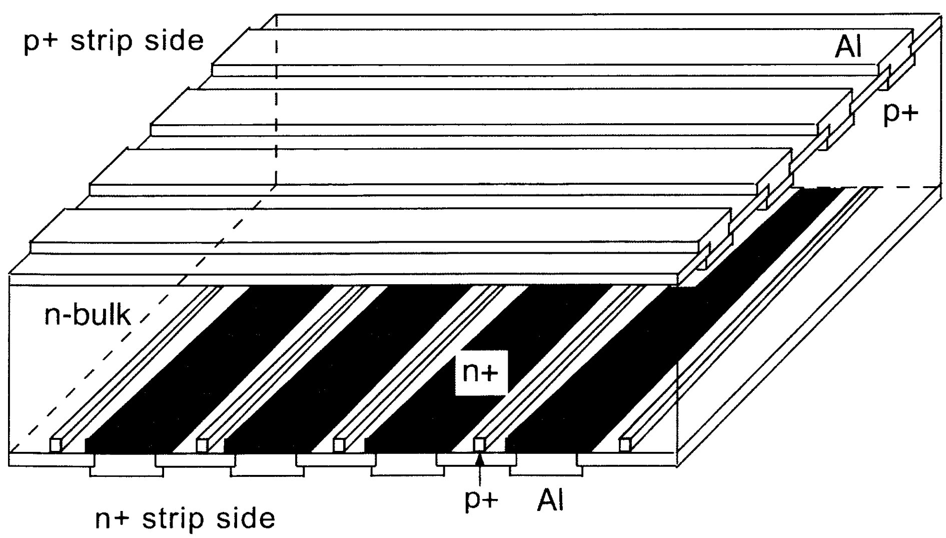

Figure 3.7: Cross-sectional view of a double sided silicon strip detector[47].

The position sensitive DSSSD is a 5 cm x 5 cm SSB detector with 16 horizontal junction elements on one side, and 16 vertical ohmic elements on the other side, creating a resolution of 256 pixels. Pixelation allows the location where the fragment hit the detector to be determined. By simultaneously recording electron and hole pulses, the DSSSD records the energy deposited in the detector by the fragment, as well as which pixel was struck.

Each pixel has an area of 9.766 mm^2, giving a well defined spatial resolution that is dependent on the arm length of the DAS. The origin of the fragment pair can be determined from the final position of both fragments. The position where the fragment struck the detector and the origin of the fragment can be used to calculate a much more accurate fragment path length than can be determined with a non-segmented silicon detector. Using a DSSSD therefore will improve the spatial resolution, leading to improved mass resolution.

3.1.5 Simulation of the SSBD

In Geant4, the SSBD is modeled by a silicon block with the same dimensions as the actual detector. In experimentation, the fragment collides with the detector giving the energy deposited by the fragment, but no position information is recovered. The maximum variation in path length using a 2 cm diameter source is 2.5% for a 20 cm arm length, and 0.4% for a 50 cm arm length. Because the fragment can have many different path lengths depending on its location of origin in the source, and the initial direction of its momentum (seen in Figure 3.6), it was necessary to determine the average path length traveled by the fragment between the two carbon foils for use in the fragment mass calculation.

Another option would be to use the center-to-center distance between the carbon foils. However, every actual fragment path length would be greater than or equal to the center-to-center distance used in the mass calculation resulting in the mass peak centered at a higher value than the actual mass of the fragment. Using the average path length that the fragment can travel correctly centers the mass peak around the fragment's actual mass.

Although the SSB detector can not be used to determine the fragment's final position, Geant4 internally tracks every particle from its creation, to its final position. I used Geant4's tracking capability to record the path length of each fragment, and store a running average. After all events in a simulation have been executed, the mass of each fragment is calculated using this average path length as the value of l in Equation 2.3.

3.1.6 Simulation of the DSSSD

In experimentation, the fragment would collide with the DSSSD giving the fragment's energy, and the DSSSD pixel that was struck. A path length corresponding to the pixel that was struck would then be used to calculate the mass of the fragment. Because of the small area of each pixel, the variation of the actual path length from the path length to the center of the pixel is less than 0.006% for a 20 cm arm length and less than 0.001% for a 50 cm arm length. Because the variation in path length is so small, the source center to pixel center path lengths were used.

The simulation was set up to use one detector simultaneously as both the SSBD and the DSSSD. For each event, the fragment's detected energy, exact path length, and pixelated path length detected by the DSSSD are stored. The exact path length is used to calculate the mass centroid detected by the SSBD (seen in Section 3.1.5), and the pixelated path length is used as the value of l in Equation 2.3 to calculate the mass of each fragment detected by the DSSSD. This way a single simulation was used to investigate the effects of changing detectors on mass resolution, without having to provide multiple Monte Carlo runs.

3.2 Particle Generator

The angle between the fission fragment trajectories after fission, known as the folding angle, contains very valuable information on the fission process, especially on the total excitation energy of the fragments[48]. The primary folding angle is 180°, however prompt emission of gamma rays and neutrons produce recoil effects, potentially changing the direction of both fragments.

The fission model built into Geant4 lacks the precision necessary to accurately model the emission of gamma particles and neutrons during a ^{252}Cf (SF) event. Improving Geant4's fission model, or developing a new model, was outside the scope of this thesis. However, an accurate model of the fission process will be incorporated into the simulation at a later date. The simulation used here was programmed to allocate the energy of fission after prompt neutron evaporation between the fragment pair based on conservation of momentum, and it was assumed that none of the energy goes into neutron, gamma, or beta production. Delayed neutron production was also ignored. Without neutron and gamma emission, the folding angle was assumed to be a constant 180°.

3.2.1 Random Particle Generator

The spontaneous fission yield libraries for ^{252}Cf are distributed by the National Nuclear Data Center (NNDC). I used the JEFF-3.1[49] library because it was the most recently updated. For each fragment, a fission yield is given. This yield must be used to bias the random particle selection in the simulation, so that each fragment has a probability of being selected that is based on its yield.

In probability and statistics, the distribution of the values of a random quantity, X, is specified in terms of its distribution function, $F(x)$, seen in Equation 3.3[50].

$$F(x) = \Pr(X \leq x) = \text{probability that}(X \leq x). \tag{3.3}$$

To get the distribution function, I numerically integrated the yield values by summing each value with all of its preceding values, and then divided by the total yield from every fragment. A plot showing the distribution function can be seen in Figure 3.8. There are many fragments with the same mass that have different atomic numbers (Z), and this can be seen as the discretization in Figure 3.8, where each grouping represents a different atomic number, and the horizontal points composing each grouping represent the different masses with the same atomic number.

To select a fragment, I programmed the simulation to generate a uniformly distributed random number between 0 and 1. This number is compared to the value of the distribution function for each fragment, starting with the first fragment in the list. If the random number is greater than the value of the distribution function, the fragment is not selected, and the random number is compared to the next fragment in the list. Once the value of the fragment's distribution function is greater than the

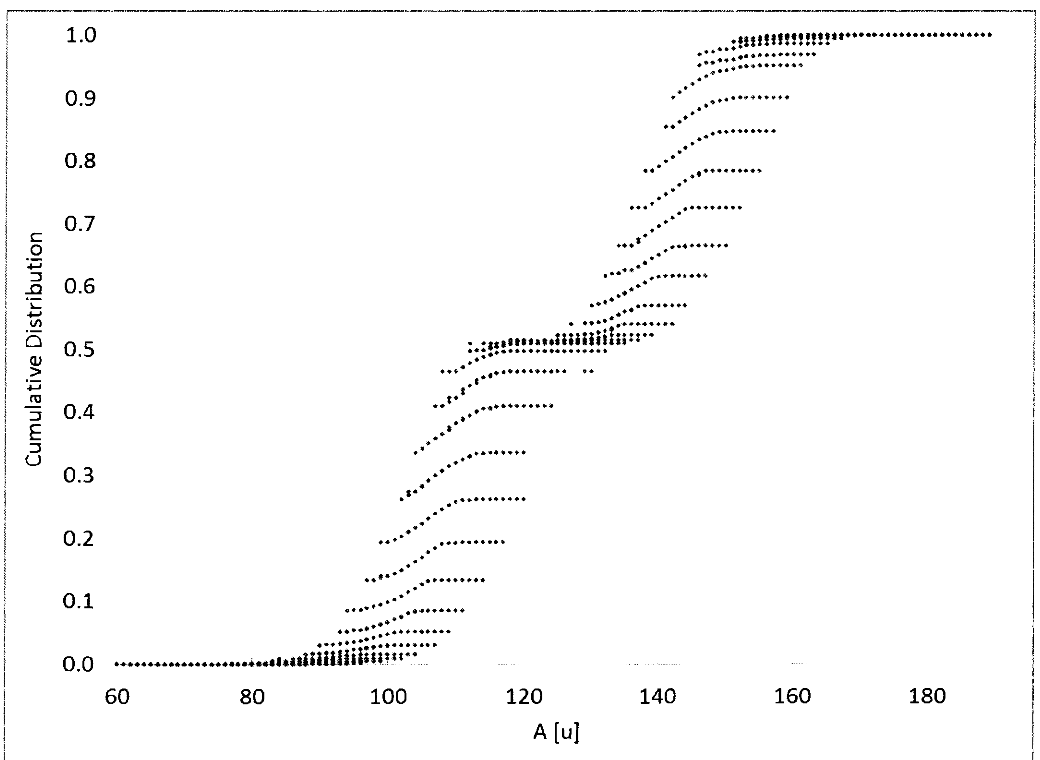

Figure 3.8: Distribution function for the fission yield of ^{252}Cf.

random number, the fragment is selected. Conservation of mass and charge is used to calculate the A and Z of the second fragment to form a pair, and the fragment pair is used by the simulation for the proceeding event. The emission of gammas and neutrons were completely neglected and need to be incorporated into the fission fragment generator at a later date.

A plot showing the yield probability from simulation using the random particle generator along with actual data from JEFF-3.1 can be seen in Figure 3.9. The two data sets are in close agreement with each other, but not exact. The discrepancies occur because prompt neutron emission is neglected by the fission generator (as previously mentioned), and the JEFF-3.1 direct fission product yield data were measured after the emission of prompt neutrons, prior to delayed neutron emission. As a secondary source, the lack of statistics from running too few fragment pairs can contribute. To reproduce the JEFF-3.1 yield spectrum exactly, it will be necessary to incorporate prompt neutron production into the fission generator at a later date. For

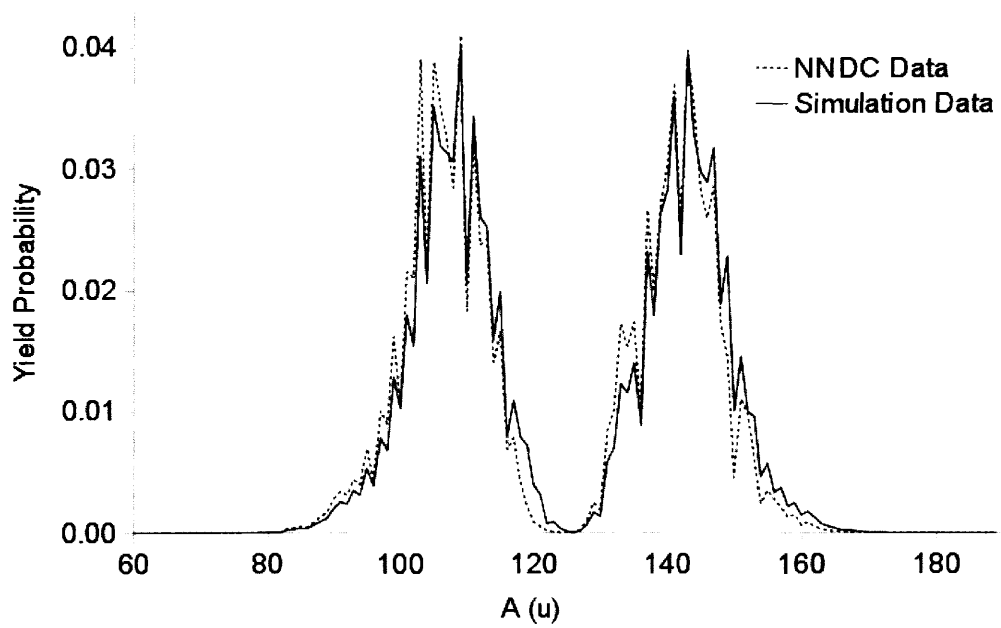

Figure 3.9: Fission yield probability of a ^{252}Cf source.

the physics we are trying to extract from the current simulation, the fission generator works sufficiently well.

The average kinetic energy released after prompt neutron emission of a ^{252}Cf (SF) event is 181.25 $\pm$ 1.3 MeV[51]. This energy is distributed among the fragments based on conservation of momentum following Equation 3.4, where E is the fragment's kinetic energy and m is its mass.

$$\frac{E_1}{E_2} = \frac{m_2}{m_1} \tag{3.4}$$

Using conservation of energy, E_2=$E_{sf,Cf}$-E_1, where $E_{sf,Cf}$ is the average kinetic energy released from a ^{252}Cf (SF) event. Using this relation, Equation 3.4 can be solved for E_1 (or E_2) seen in Equation 3.5, where A_{Cf} is the atomic mass of ^{252}Cf.

$$E_1 = E_{sf,Cf}\left(\frac{m_2}{A_{Cf}}\right) \tag{3.5}$$

The General Particle Source (GPS) toolkit provided as a part of Geant4 has the functionality to apply a Gaussian energy distribution to the fragments. The GPS generates a Gaussian energy spectrum with a mean value of 181.25 MeV, and a FWHM of 1.3 MeV. The energy emitted from fission after prompt neutron emission is randomly extracted from the Gaussian spectrum, and split between the fragment pair using Equation 3.4. A plot of the detected fragment kinetic energy as a function of mass can be seen in Figure 3.10.

The statistical fluctuation in the energy of fission can be seen in Figure 3.10 by the vertical lines at each discrete mass value, which represent the fluctuation in energy for each mass.

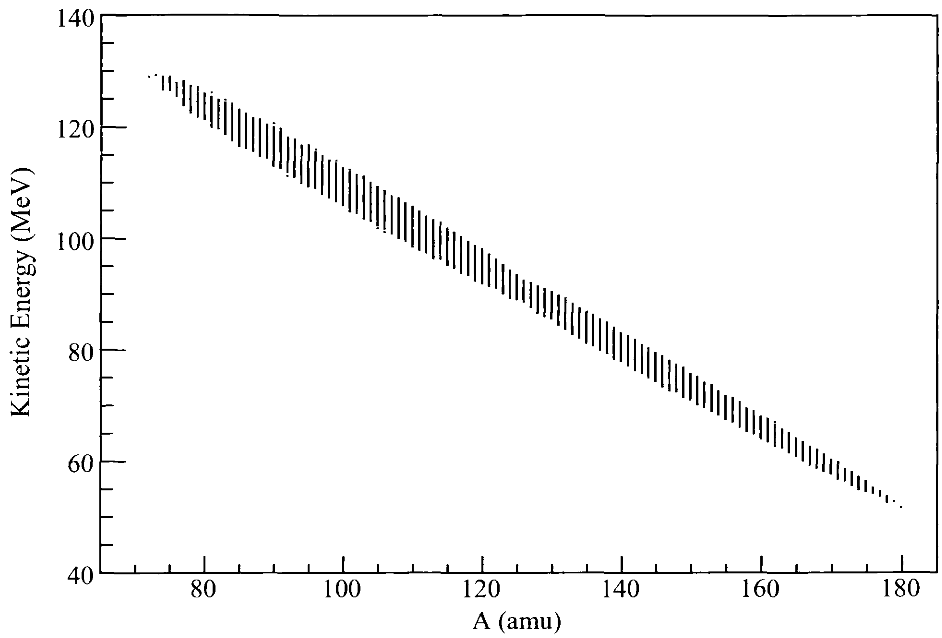

Figure 3.10: Kinetic energy as a function of mass.

3.2.2 Fragment Pair Generator

To determine the mass resolution from the simulation, the calculated fragment mass values for each fission fragment were histogrammed individually. A Gaussian fit was performed on each histogram providing the mass resolution from simulation. The simulation was run for 5x10^6 fission events for a single fragment pair to achieve acceptable statistics.

There are 566 different fragment pairs for ^{252}Cf listed in the JEFF-3.1 library. The smallest difference in the distribution function between fragments is 1.23×10^{-13}. The random generator would have to run around 10^{17} fragment pairs in order to generate reasonable statistics. For this reason, using the random particle generator to determine the mass resolution would at this point be extremely inefficient and time consuming.

The source was programmed with an option to use a specific fragment pair for every event simulated, allowing me to minimize the computing time necessary to get adequate statistics for the mass resolution. The fragment pairs selected for the simulation were chosen to be representative of the entire mass spectrum to show how the resolution changes as a function of mass.

3.3 Particle Source

To define a source, the GPS requires defining the initial position and momentum direction of the fragment. The programming methodology of the particle source is presented in Sections 3.3.1 and 3.3.2.

3.3.1 Initial Fragment Position

The GPS was programmed to randomly generate the initial position of the fragment inside the volume of several predefined cylinders, introducing two types of uncertainty into the simulation: variation in fragment origin leading to uncertainty in fragment path length, and energy straggling in the source leading to uncertainty in the detected energy of the fragment. The contribution of each to the mass resolution was then investigated. The dimensions of the cylinders used are found in Table 3.1.

The initial position of each fragment pair was stored and a check on uniform fragment generation was performed. A plot of the x-y position of origin of each fragment pair can be seen in Figure 3.11 for verification.

As source diameter increases, uncertainty in the origin of the fragment increases.

Table 3.1: Dimensions of source cylinders.

Source Thickness (μg/cm^2)	Source Diameter (mm)
100	5
-	10
-	20
200	5
-	10
-	20

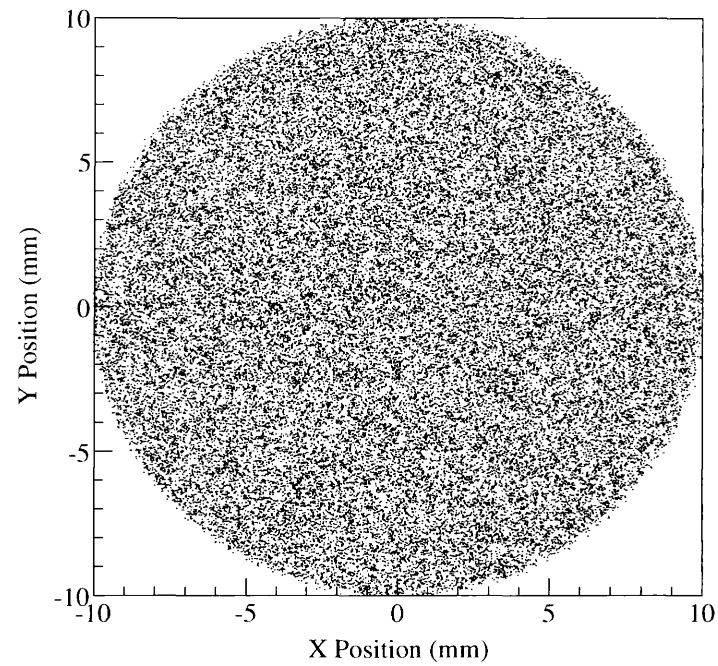

Figure 3.11: Fragment pair x-y position of origin in the source.

With the DSSSD it is possible to determine the starting position of the fragment, therefore increasing source diameter has no effect on the spatial resolution. With the SSBD, no position information is given, therefore the spatial resolution degrades with increasing source diameter, leading to degradation in mass resolution.

Increasing source thickness also introduces uncertainty in the axial origin of the particle, which an SSBD is unable to determine, however the effect is small enough to be assumed negligible. As the source thickness increases, energy straggling of the fragment in the source increases. This leads to uncertainty in the energy detected by the silicon detector, regardless of detector type, which leads to degradation in mass resolution. Increasing the source thickness also increases the flux of particles into the active solid angle. A compromise between mass resolution and yield needs to be pursued.

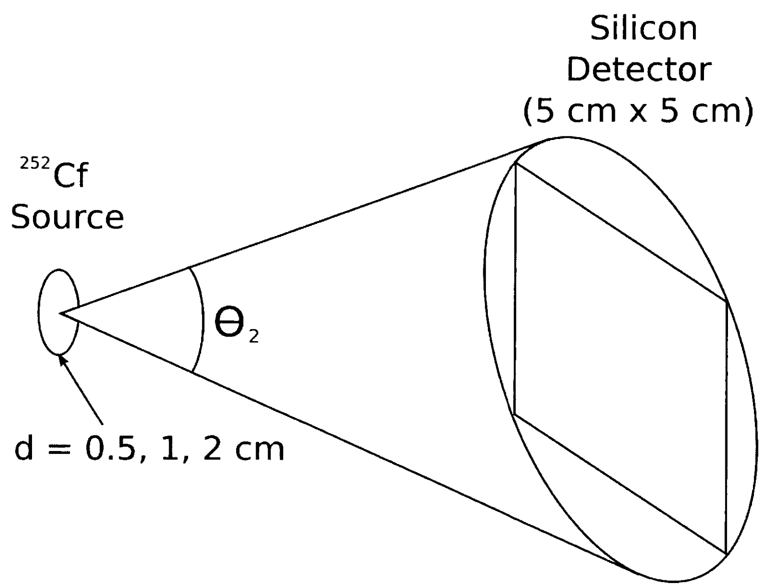

Figure 3.12: Restricted source emission.

3.3.2 Fragment Momentum Direction

By default, the GPS is configured to simulate emission from the source isotropically. This represents the most realistic source emission. However, the vast majority of fragments are emitted outside of the solid angle of the detector providing no useful information to the simulation, wasting large amounts of computing time. To utilize as much computational time as possible, I restricted the emission of the source to a cone seen in Figure 3.12.

For each event, a random angle, θ_1 is generated between 0 and 180 degrees. In the simulation, the momentum direction of the particle is defined as a vector in cartesian coordinates, with an x, y, and z component. Each component is defined in Equation 3.6, where θ_2 is defined in Figure 3.12, and $zGun$ is the distance from the source to the silicon detector.

$$\begin{aligned} x &= Sin(\theta_2) * Cos(\theta_1) * zGun \\ y &= Sin(\theta_1) * Sin(\theta_2) * zGun \\ z &= Cos(\theta_2) * zGun \end{aligned} \tag{3.6}$$

The size of the cone is chosen so that the entire surface area of the silicon detector is enclosed by it. The source emits into the solid angle defined by Equation 3.6, allowing the data collection rate to increase significantly compared to an isotropic source. A check on the uniformity of emission from the source was performed by plotting the final x-y position of fragment deposition in the silicon detector. This plot can be seen in Figure 3.13(a), and shows anisotropy in the emission of fragments from the source. This anisotropy will cause an unrealistic representation of the variation in path length of the fragment resulting in an underestimation of the mass resolution. For this reason, the method of restricting source emission to a cone was not pursued further.

The GPS toolkit has however an alternative functionality to limit the angular distribution from the source while still providing isotropic emission. This method was used to limit emission from the source to a plane imposed on a sphere by imposing minimum and maximum values for the angles θ and ϕ in the cylindrical coordinate

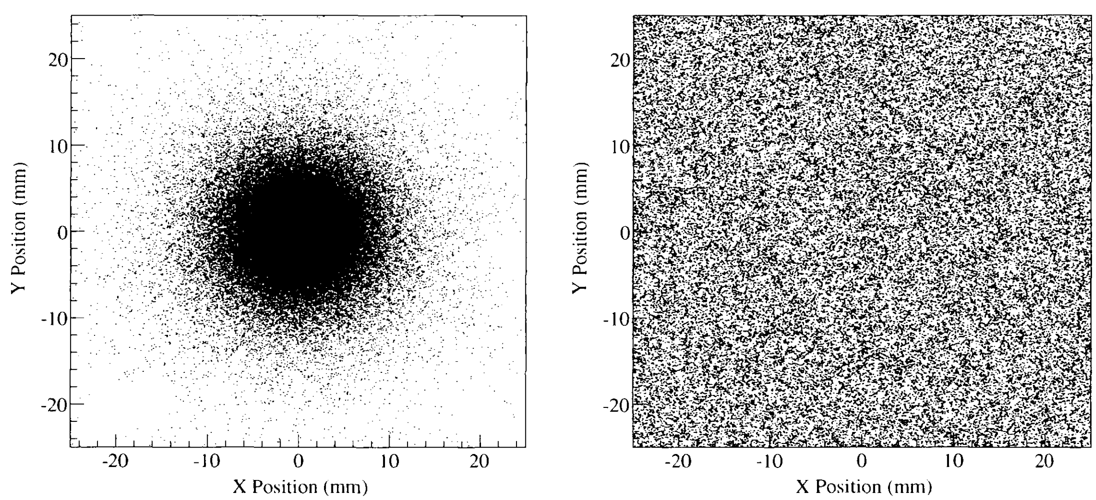

(a) Source emission limited to a cone

(b) Source emission limited to a plane imposed on a sphere

Figure 3.13: Final simulated position of fission fragment deposition in the SSBD.

system. The angles were chosen to allow every fragment, regardless of its position of origin in the source, to have the potential to impact any point on the silicon detector. A check on the uniformity of emission from the source can be seen in Figure 3.13(b), and clearly shows uniform illumination of the silicon detector indicating isotropic source emission.

3.4 Simulation Parameters

A detailed schematic of the simulation input parameters can be seen in Figure 3.14. The values used for all of the parameters in Figure 3.14 can be seen in Table 3.2. The input variables seen in Table 3.2 that are fixed are hard-coded into the simulation. The input variables that can change are entered by the user when calling the program.

The simulation is performed and output parameters seen in Table 3.3 are stored for post-processing with ROOT. The energy deposited by each fragment in the outer

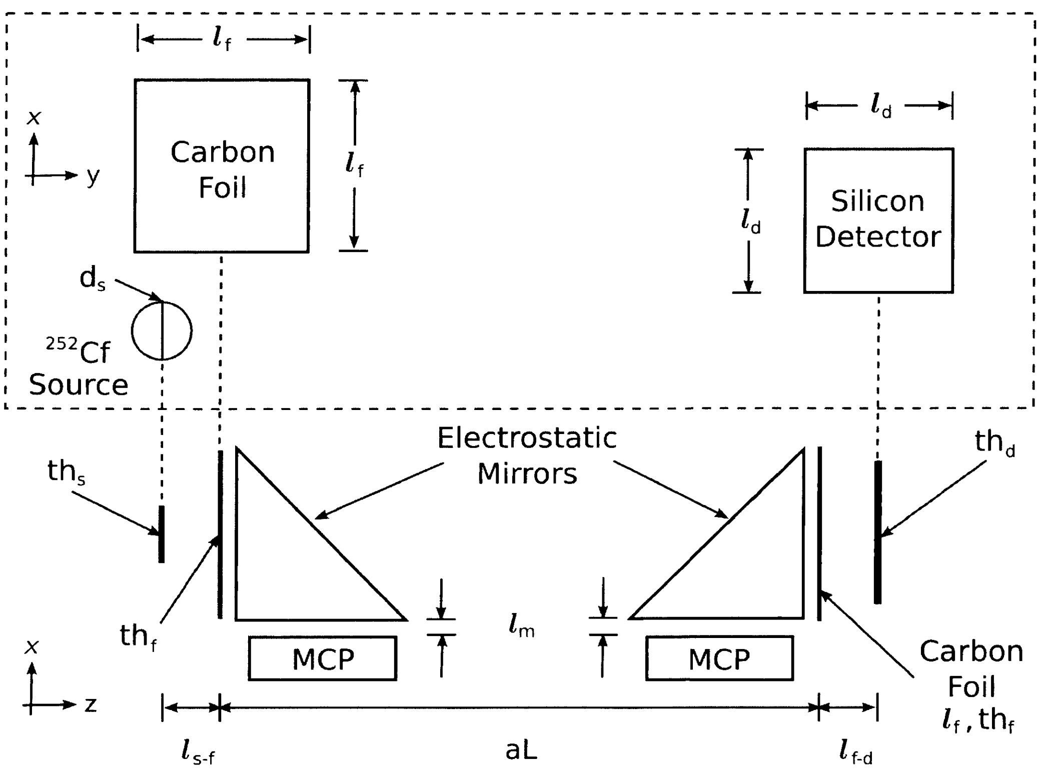

Figure 3.14: Schematic of simulation input parameters for one arm of a DAS.

Table 3.2: Simulation input parameters and their description.

Input Parameter	Value(s)	Description
d_s	5,10,20 mm	Diameter of the ^{252}Cf source.
th_s	100,200 $\mu g/cm^2$	Thickness of the ^{252}Cf source.
l_f	6 cm	Side length of both inner and outer carbon foils.
th_f	10,20,30 $\mu g/cm^2$	Thickness of both inner and outer carbon foils.
l_{s-f}	4 mm	Distance between the ^{252}Cf source and inner carbon foil.
aL	20,30,40,50 cm	Distance between the carbon foils (arm length of the DAS).
l_{f-d}	4 mm	Distance between the outer carbon foil and the silicon detector.
l_m	1 mm	Distance between the MCP and the electrostatic mirror.
l_d	5 cm	Side length of the silicon detector.
th_d	150 μm	Thickness of the silicon detector.

carbon foil, E_{f2}, was averaged and used as the value of $E_{f,ave}$ in Equation 2.3. The time of flight of each fragment was calculated by taking the difference between the stored time signals (t_{f1} and t_{f2}) and was used as the value of t in Equation 2.3. The various positions seen in Table 3.3 that are stored by the simulation were used to calculate the exact path length of every fragment, in order to determine the average path length travelled by all of the fragments, l_{ave}.

The fragment mass detected by the SSBD was calculated using the average path length as the value of l in Equation 2.3. The fragment mass detected by the DSSSD

Table 3.3: Simulation output parameters and their description.

Output Parameter	Description
x_0, y_0, z_0	Initial position of the fragment in the ^{252}Cf source.
x_{f1}, y_{f1}, z_{f1}	Position of fragment collision with the inner carbon foil.
x_{f2}, y_{f2}, z_{f2}	Position of fragment collision with the outer carbon foil.
x_{SD}, y_{SD}, z_{SD}	Final position of fragment deposited in the silicon detector.
x_{seg}, y_{seg}, z_{seg}	Position of the center of the pixel of the DSSSD struck by the fragment.
t_{f1}	Time of fragment collision with the inner foil.
t_{f2}	Time of fragment collision with the outer foil.
M	Exact mass of the fragment.
Z	Nuclear charge (number of protons) of the fragment.
E_0	Initial kinetic energy carried by the fragment.
E_{f1}	Energy deposited by the fragment in the inner carbon foil.
E_{f2}	Energy deposited by the fragment in the outer carbon foil.
E_{SD}	Energy deposited by the fragment in the silicon detector.

was calculated by using the final position of the fragment (x_{seg} and y_{seg}) to identify which pixel was struck. The position of the center of the pixel was used as the final position of the fragment to calculate the segmented path length, l_{seg}, which was used as the value of l in Equation 2.3.

CHAPTER 4

ANALYSIS

In this chapter I describe the software and procedures used to perform the error analysis. A detailed description of each source of error is given as well as calculations of my anticipated error. Solid angle approximations are also made to investigate the effects of changing simulation parameters.

4.1 Error Analysis

Geant4 was used in conjunction with ROOT[52], a data analysis framework developed by CERN. ROOT provides the functionality needed to analyze large amounts of data in an efficient way, by defining data as a set of objects. This allows direct access to specific attributes of selected objects, without analyzing the rest of the data.

Bash scripts were used to run all Geant4 simulations. Execution of a single script ran each simulation, changing variables between simulations, and saving the ROOT output file for each simulation automatically. A separate script performed the mass calculations for each fragment and histogrammed the results.

A ROOT script was written to post-process the histograms that were created. The macroscript reads the histograms from the ROOT file and performs Gaussian fits (internal ROOT function) on each mass histogram. The script saves a copy of the histogram, and exports the fit data into a text file. The text file was later imported into OpenOffice for error analysis and plotting.

The mean from the Gaussian fit of each histogram represents the calculated mass of the fragment, and the sigma represents the variance in the calculated mass of the fragment. The full width half maximum (FWHM) of the Gaussian was calculated using Equation 4.1[53].

$$\text{FWHM} = 2\sqrt{2 \times \ln(2)} \times \sigma \tag{4.1}$$

The FWHM from the simulation takes into account the following sources of error:

- Variations in flight path due to changing source diameter and thickness
- Variation in flight path due to changes in DAS arm length
- Energy straggling in the source due to variation in source thickness
- Energy straggling of the fission fragment in the carbon foil

However, the error from the simulation does not incorporate the energy resolution of the silicon detector (same for SSBD as DSSSD), or the timing resolution of the MCPs. Because the simulation implicitly accounts for multiple sources of error, not just the error due to variations in flight path, the error propagation found in Equation 2.2 needs to be modified.

Following the methodology presented by Knoll[45], the overall mass resolution can be calculated by adding the uncertainty from the simulation with the uncertainty from the instrumentation in quadrature, seen in Equation 4.2, where A_s is the calculated mass value from simulation, and ΔA_s is the uncertainty in the calculated mass.

$$\frac{\Delta A}{A} = \left[\left(\frac{\Delta E}{E}\right)^2 + 2\left(\frac{\Delta t}{t}\right)^2 + \left(\frac{\Delta A_s}{A_s}\right)^2\right]^{1/2} \tag{4.2}$$

4.2 Estimated Error

To estimate the range of uncertainty in mass resolution to be expected from simulation, calculations were performed in Mathematica[54]. SRIM[55], a software package for calculations dealing with the transport of ions through matter, was used to estimate the energy loss of fission fragments in the ^{252}Cf source, as well as the energy loss of fission fragments in carbon foils.

The lower bound of the achievable mass resolution was estimated by including only error sources from instrumentation. Uncertainty due to energy loss and straggling of the fission fragments, as well as uncertainty due to variations in the flight path of the fission fragments were neglected. The upper bound of the mass resolution was estimated by approximating the maximum error contribution from all error sources.

4.2.1 Energy Loss and Straggling

SRIM does not have the capability of simulating ion interactions with ^{252}Cf source material. To estimate the energy loss of fission fragments in the source, SRIM was used to simulate the energy loss of fission fragments passing through ^{231}Pa, ^{232}Th, and ^{238}U sources. The energy loss data from SRIM was imported into Mathematica for analysis. The data was first histogrammed, and then fit with a Gaussian curve. An example histogram of the energy lost in the source by a fragment of mass 84 generated uniformly in the ^{238}U source can be seen in Figure 4.1.

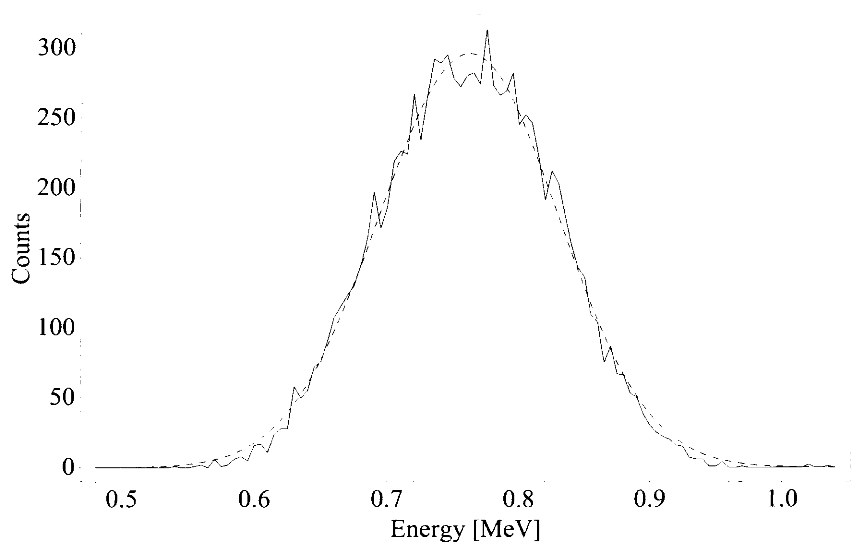

Figure 4.1: Histogram of the energy lost by a fission fragment with A = 84 traveling out of a ^{238}U source, with the Gaussian fit overlayed (dashed line).

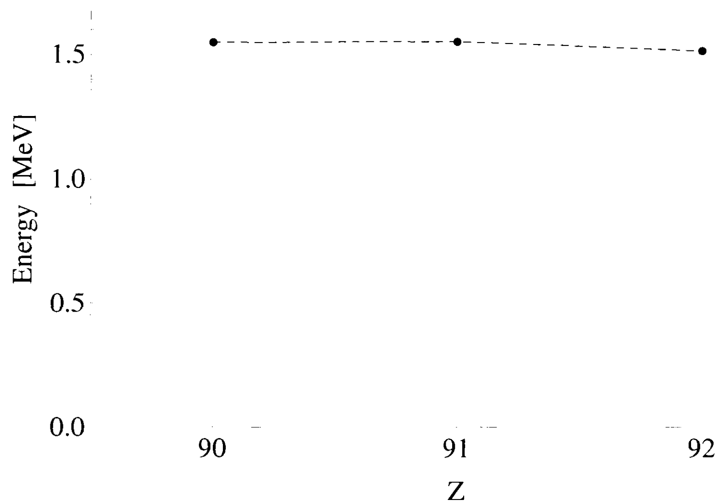

Figure 4.2: Energy loss of a fission fragment with A = 84 as a function of the atomic number (Z) of the source, for ^{231}Pa, ^{232}Th, and ^{238}U sources.

The mean from the Gaussian fit represents the average energy lost by the fission fragment, E_l, and the FWHM of the Gaussian fit represents the uncertainty in the energy loss, or ΔE_l. The mean energy loss for the ^{231}Pa, ^{232}Th, and ^{238}U sources was then plotted as a function of atomic number, seen in Figure 4.2, for the purpose of extrapolating the energy loss in a ^{252}Cf source.

As seen in Figure 4.2, the energy loss does not significantly change for small variations of Z. For the purpose of an approximation, I assumed that the energy lost by fission fragments through a ^{252}Cf source was roughly the same as the ^{231}Pa, ^{232}Th, and ^{238}U sources, and therefore the uncertainty in the energy loss was also roughly the same. This process was repeated using fission fragments of the same masses as used in simulation (A=84,112,140,168).

Simulations using SRIM were also used to estimate the energy loss of fission fragments in carbon foils with thicknesses of 10, 20, and 30 μg/cm^2 using the same methodology, except no extrapolation was necessary. An example histogram of a fission fragment of A = 84 through a 10 μg/cm^2 carbon foil can be seen in Figure 4.3, with the Gaussian fit overlayed (dashed line).

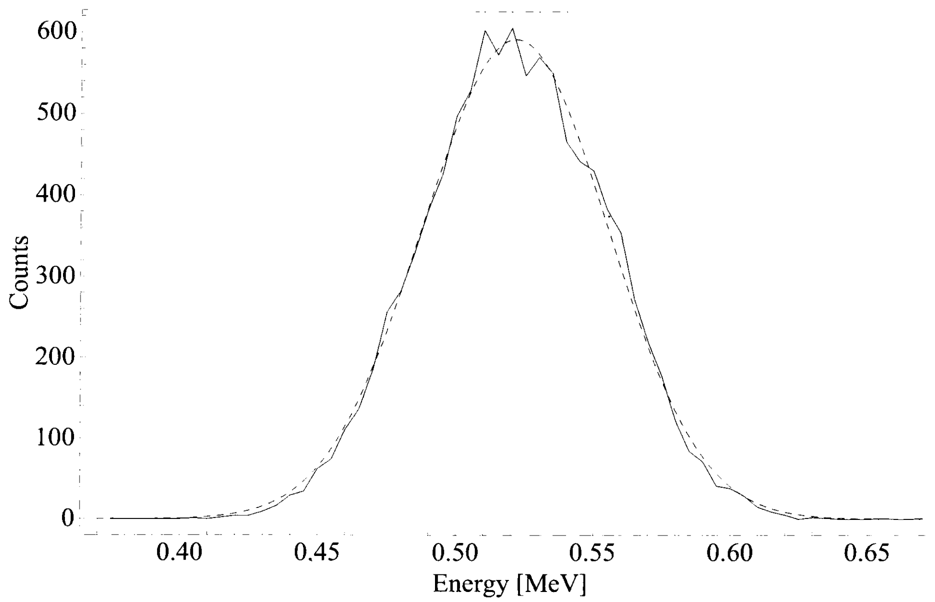

Figure 4.3: Histogram of the energy loss of a fission fragment with A = 84 through a 10 μg/cm^2 carbon foil, with the Gaussian fit overlayed (dashed line).

Energy straggling, ΔE_s, was estimated to be 10% of the energy loss, or $0.1{*}E_l$. The error due to energy loss and straggling of fission fragments in the source and in carbon foils, ΔE, was determined using Equation 4.3.

$$\Delta E = \sqrt{\left(\Delta E_l{}^2 + \Delta E_s{}^2\right)_{Source} + 2\left(\Delta E_l{}^2 + \Delta E_s{}^2\right)_{Foil}} \tag{4.3}$$

4.2.2 Flight Path

Uncertainty in the fission fragment's flight path was estimated by determining the maximum difference between the flight path of a fragment that strikes the center of a pixel of the DSSSD, and the flight path of a fragment that strikes the corner of a pixel of the DSSSD. The equation for the maximum error due to uncertainty in the flight path, Δl, can be seen in Equation 4.4, where aL represents the arm length of the DAS in mm, and 2.20971 mm is the center to corner distance of a pixel.

$$\frac{\Delta l}{l} = \frac{\sqrt{\mathrm{aL}^2 + 2.20971^2} - \mathrm{aL}}{\mathrm{aL}} \tag{4.4}$$

There is also uncertainty in the measurement of the DAS arm length, Δl_m, which is assumed to be 0.5 mm.

4.2.3 Estimated Mass Resolution

The estimated overall mass resolution was calculated using Equation 4.5, which was developed using the methodology presented by Knoll[45].

$$\frac{\Delta A}{A} = \sqrt{\left(\frac{\Delta E}{E_o}\right)^2 + \left(2\frac{\Delta l}{\mathrm{aL}}\right)^2 + \left(2\frac{\Delta l_m}{\mathrm{aL}}\right)^2 + \left(2\frac{\Delta t}{t}\right)^2 + \left(\frac{\Delta E_{SSB}}{E_o}\right)^2} \tag{4.5}$$

The results from the error estimations with timing resolutions of 100 ps and 200 ps can be seen in Figure 4.4, and Figure 4.5 respectively. In each plot, the bottom solid line represents the estimated lower limit of the mass resolution, the bottom dotted line represents the simulation results for the configuration which yielded the lowest mass resolution, the upper dotted line represents the simulation results for the configuration which yielded the highest mass resolution, and the top solid line represents the estimated upper limit of the mass resolution. The shaded region represents the area of all the simulation data, and it is clear that all of the data from simulation falls within the bounds of the estimated error.

4.2.4 Estimate of Useful Detector Timing Resolution

The velocity, v, of a fission fragment is given by Equation 4.6, where E and m are the energy and mass of the fragment respectively.

$$v = \sqrt{\frac{2E}{m}} \tag{4.6}$$

If the mass is assumed constant, the relative uncertainty in the velocity, $\Delta v/v$, is

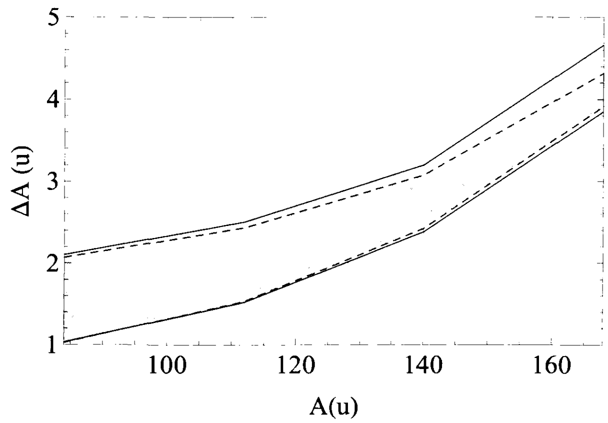

(a) 10 μg/cm^2 foil

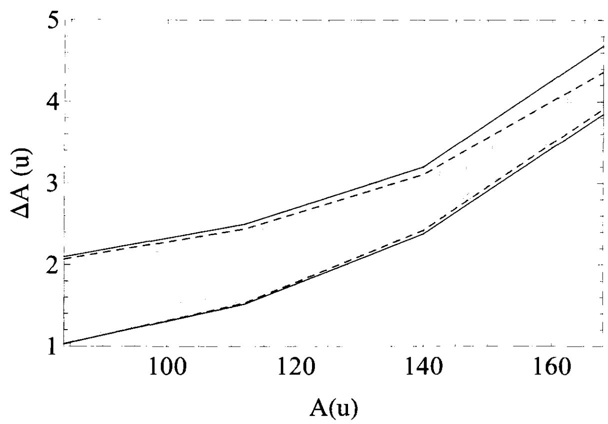

(b) 20 μg/cm^2 foil

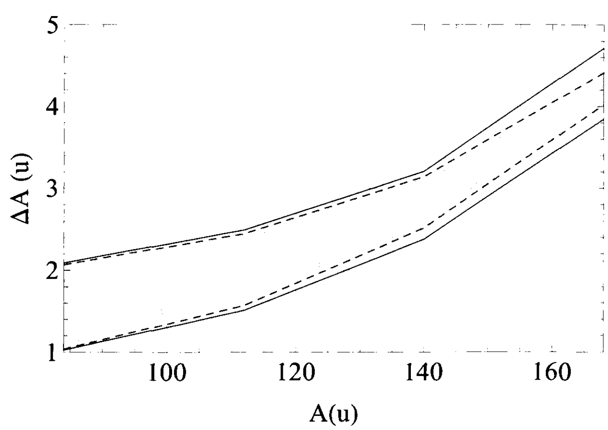

(c) 30 μg/cm^2 foil

Figure 4.4: Comparison between estimated and simulated mass resolution with a timing resolution of 100 ps.

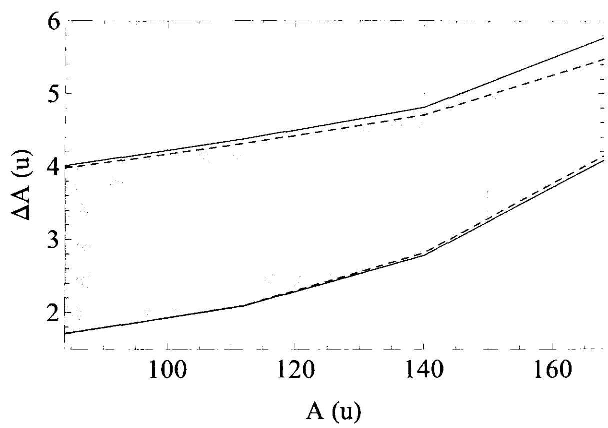

(a) 10 μg/cm^2 foil

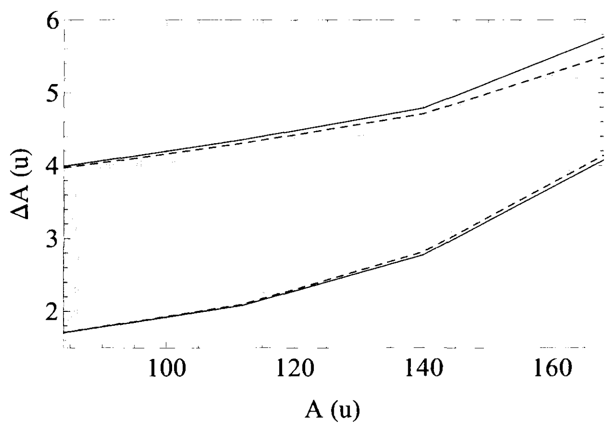

(b) 20 μg/cm^2 foil

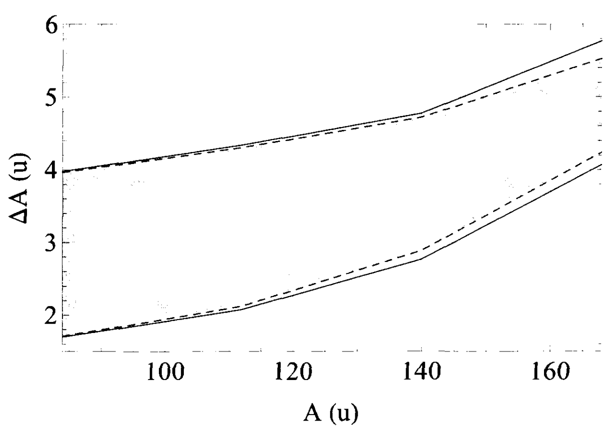

(c) 30 μg/cm^2 foil

Figure 4.5: Comparison between estimated and simulated mass resolution with a timing resolution of 200 ps.

given by Equation 4.7.

$$\frac{\Delta v}{v} = \frac{1}{2}\frac{\Delta E}{E_o} \tag{4.7}$$

The flight time, t, can be calculated using Equation 4.8, where l is the distance the fission fragment traveled in time t.

$$t = \frac{l}{v} \tag{4.8}$$

From Equation 4.8, it follows that the uncertainty in the flight time, Δt, is given by Equation 4.9.

$$\frac{\Delta t}{t} = \sqrt{\left(\frac{\Delta v}{v}\right)^2 + \left(\frac{\Delta l}{\mathrm{aL}}\right)^2} \tag{4.9}$$

The uncertainty in flight time can be approximated by combining Equation 4.9 with Equation 4.7 to get Equation 4.10.

$$\frac{\Delta t}{t} = \sqrt{\left(\frac{1}{2}\frac{\Delta E}{E_o}\right)^2 + \left(\frac{\Delta l}{\mathrm{aL}}\right)^2} \tag{4.10}$$

The estimated range of uncertainty in the flight time for different foil thickness can be seen in Figure 4.6. A detector timing resolution of 100 ps is clearly useful for all foil thicknesses. A detector timing resolution of 200 ps would be a limiting factor in the experiment. Equation 4.10 implies that the uncertainty in flight time is related to the uncertainty in the energy of the fission fragment. Even if the MCPs had instantaneous response with zero uncertainty, a timing resolution lower than what is seen in Figure 4.6 is unachievable. It makes therefore sense to achieve instrumental (MCP) resolution of the order of 100 ps, but trying to improve on that would have limited effect.

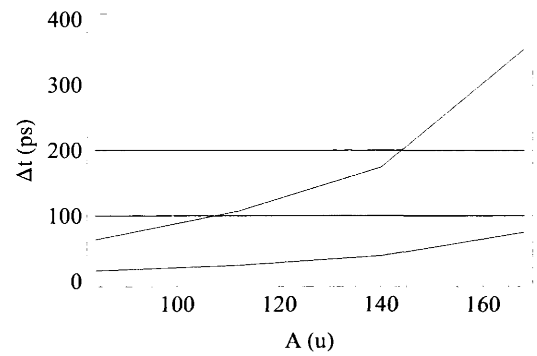

(a) 10 μg/cm^2 foil

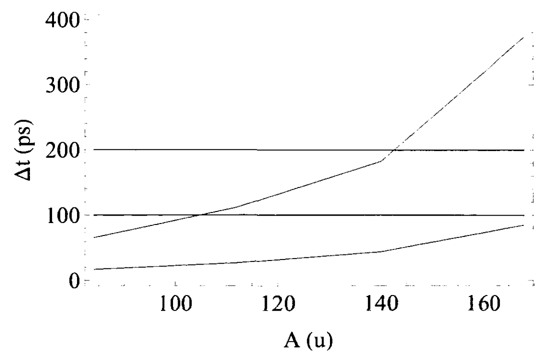

(b) 20 μg/cm^2 foil

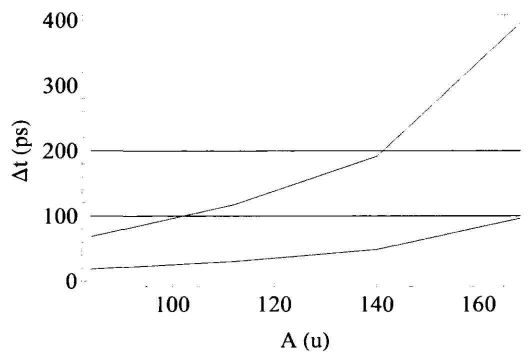

(c) 30 μg/cm^2 foil

Figure 4.6: Estimated range of uncertainty in flight time.

4.3 Solid Angle

The solid angle from a circular disk emitting isotropically, aligned with a circular disk detector is given by Equation 4.11, where a, s, and d are the detector radius, source radius, and the distance between the two, respectively. The dimension of the second carbon foils were chosen so that the silicon detector would be the limiting factor on solid angle (see Table 3.2). For the purpose of estimating fluctuations in solid angle for changing parameters, the silicon detector was assumed to be a circular disk.

$$\Omega = \frac{4\pi a}{s} \int_0^\infty \frac{\exp(-dk) J_1(sk) J_1(ak)}{k} dk \tag{4.11}$$

Table 4.1: Solid angle for changing DAS arm length and source diameter.

Source Diameter (mm)	Arm Length (cm)	Solid Angle (mSr)
5	20	79.59
-	30	38.00
-	40	22.14
-	50	14.47
10	20	79.57
-	30	38.00
-	40	22.14
-	50	14.47
20	20	79.48
-	30	37.97
-	40	22.13
-	50	14.47

This integral does not have an analytical solution, therefore a numerical approximation seen in Equation 4.12 was used to calculate the solid angle of the DAS, where $J_1(x)$ are Bessel functions of x[45]. The solid angle for the source diameters and arm lengths simulated can be seen in Table 4.1.

$$\begin{aligned}
\Omega &\cong 2\pi\left[1 - \frac{1}{(1+\beta)^{1/2}} - \frac{3}{8}\frac{\alpha\beta}{(1+\beta)^{5/2}} + \alpha^2[\mathrm{F1}] - \alpha^3[\mathrm{F2}]\right] \\
\mathrm{F1} &= \frac{5}{16}\frac{\beta}{(1+\beta)^{7/2}} - \frac{35}{64}\frac{\beta^2}{(1+\beta)^{9/2}} \\
\mathrm{F2} &= \frac{35}{128}\frac{\beta}{(1+\beta)^{9/2}} - \frac{315}{256}\frac{\beta^2}{(1+\beta)^{11/2}} + \frac{1155}{1024}\frac{\beta^3}{(1+\beta)^{13/2}}
\end{aligned} \tag{4.12}$$

where

$$\alpha = \left(\frac{s}{d}\right)^2 \qquad \beta = \left(\frac{a}{d}\right)^2$$

The decrease in solid angle moving from a 5 mm source diameter to a 20 mm source diameter is less than 0.14 % for all arm lengths. It is clear that increasing the source diameter has a negligible effect on the solid angle of the DAS. However, it does allow an increase in the count rate of the source at a given source thickness, therefore the largest possible source diameter is desired if this does not decrease the mass resolution.

CHAPTER 5

RESULTS

In this chapter, the results for the SSBD and the DSSSD are summarized. For each detector type, the effect on mass resolution from varying each parameter from simulation is described. After summarizing the results, a final detector design is suggested and areas of future work are outlined.

5.1 Silicon Surface Barrier Detector

A histogram of the path length of every fragment from simulation with a 20 mm source diameter, a source thickness of 100 μg/cm^2, a foil thickness of 10 μg/cm^2, and a 20 cm arm length for A = 84 can be seen in Figure 5.1, with the y-axis plotted logarithmically.

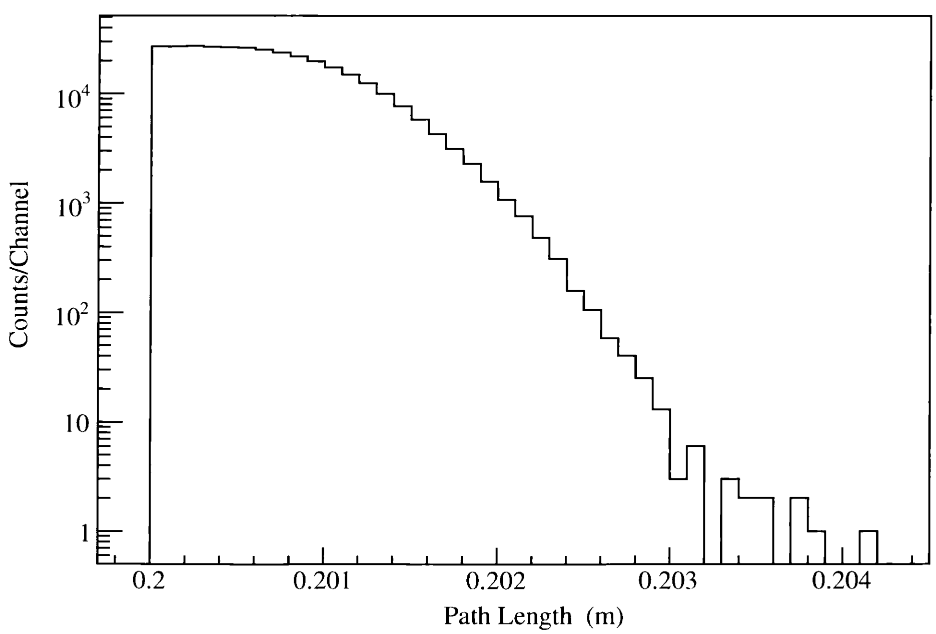

Figure 5.1: Fragment path length from simulation with A = 84, 100 μg/cm^2 source thickness, 20 mm source diameter, 10 μg/cm^2 foil thickness, and 20 cm arm length with the y-axis plotted logarithmically.

It is possible for a fission fragment to take the shortest possible path length from the source to the detector regardless of the location where the fragment originates in the source. However, for a particle to take the longest possible path length from the source to the detector it can only originate on the radial edge of the source and must deposit near the opposite edge (in the x-y direction) of the silicon detector. It is much more likely for a particle to travel a shorter distance than the median path length as can be seen in Figure 5.1. Note that with more statistics, Figure 5.1 would show path lengths up to 20.05 cm, however the probability of a fragment taking this path length is extremely low.

The effect of the mean path length being less than the median path length can be seen best in Figure 5.2, which is a histogram from simulation with A = 84, a 20 mm source diameter, a source thickness of 100 μg/cm^2, a foil thickness of 10 μg/cm^2, and a 20 cm arm length with the y-axis plotted logarithmically.

As seen in Equation 2.3, the calculated mass of the fragment is proportional to

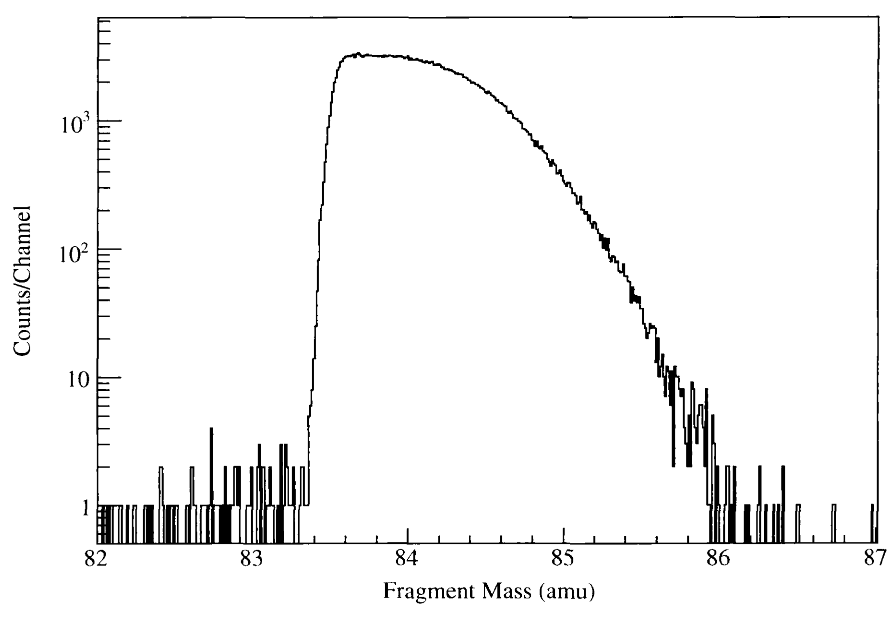

Figure 5.2: Simulation results for A = 84, 100 μg/cm^2 source thickness, 20 mm source diameter, 10 μg/cm^2 foil thickness, and a 20 cm arm length with the y-axis plotted logarithmically.

the square of the time of flight. When a fragment travels the longest possible path length, the path length used to calculate the mass is underestimated resulting in an overestimation of the calculated mass, and asymmetry in the mass histogram. This is seen most prominently as the trailing edge in Figure 5.2.

Histograms from simulation with a source diameter of 20 mm, a source thickness of 100 μg/cm^2, and a foil thickness of 10 μg/cm^2 for A = 84 can be seen in Figure 5.3. If the data does not take the form of a Gaussian it becomes much more difficult to analyze. With symmetric data, the FWHM of the Gaussian represents the mass resolution from simulation. With asymmetric data, the FWHM is not meaningful

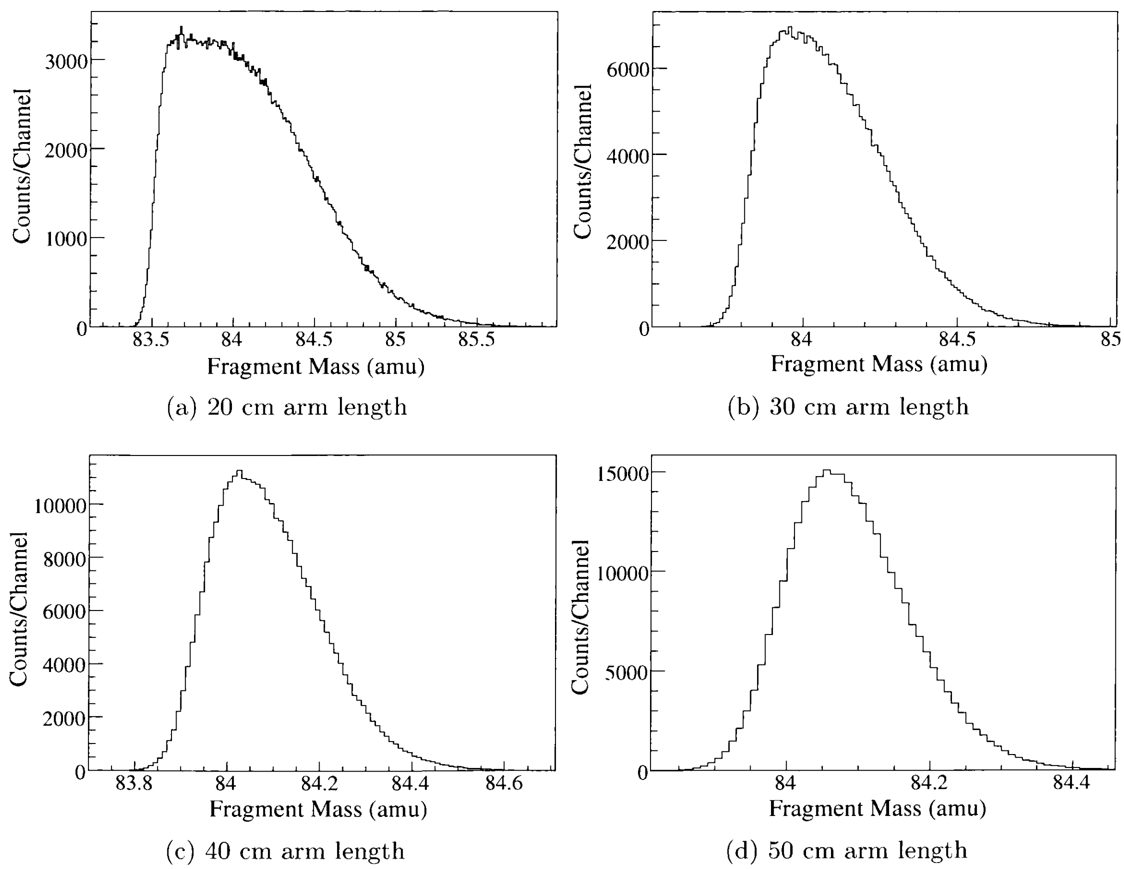

Figure 5.3: Simulation results for A = 84, and a source diameter of 20 mm with a solid SSBD.

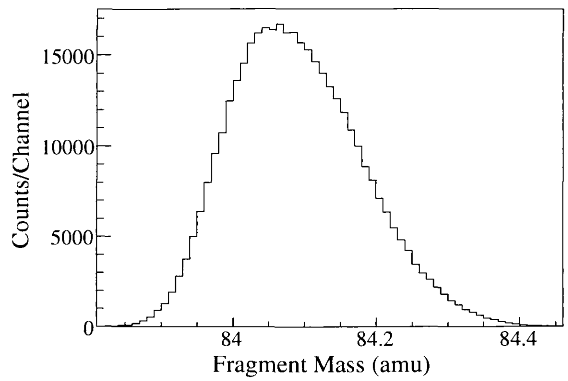

Figure 5.4: Simulation results for A = 84, a 100 μg/cm^2 source thickness, 5 mm source diameter, 10 μg/cm^2 foil thickness, and 50 cm arm length.

for comparison with symmetric data (from the DSSSD). Even with the simulation parameters configured for optimal mass resolution (100 μg/cm^2 source thickness, 5 mm source diameter, 10 μg/cm^2 foil thickness, and 50 cm arm length) the mass histogram is asymmetric as can be seen in Figure 5.4.

This simulation has shown that it is difficult to reconcile large solid angle and mass resolution with a nonsegmented detector. For this reason, a DSSSD or some type of position sensitive detector is recommended.

5.2 Double Sided Silicon Strip Detector

The simulation with double sided silicon strip detectors was used to investigate the effects of 4 variables on the mass resolution of the DAS:

- Source Thickness
- Source Diameter
- Foil Thickness
- DAS Arm Length

The effect of each are discussed in this section, along with the simulation results. With 4 simulation variables changing, there was a large amount of data generated.

To determine the impact of each variable, the data was plotted with one changing variable while the rest of the variables remained constant.

Initially, the data was plotted using the paramater configuration that produced the best mass resolution, Configuration A, and the configuration that produced the worst mass resolution, Configuration B. More configurations were investigated as needed. Configuration A has a source thickness of 100 μg/cm^2, a source diameter of 5 mm, a foil thickness of 10 μg/cm^2, and an arm length of 50 cm. Configuration B has a source thickness of 200 μg/cm^2, a source diameter of 20 mm, a foil thickness of 30 μg/cm^2, and an arm length of 20 cm.

5.2.1 Source Thickness

The more source material, the higher the count rate of the source. The higher the count rate, the faster data is acquired with the DAS. However, the more source material, the more energy loss and straggling the fragment experiences in the source. Energy loss and straggling in the source cannot be detected, introducing uncertainty in the detected energy of the fragment. The energy lost by the fragment before the MCP registers the first time signal does not correspond to the measured velocity of the fragment. Therefore, the thickness of the source was not expected to influence the mass resolution.

The mass resolution from simulation, without error contributions from instrumentation (MCP timing and DSSSD energy), varied only on the order of 0.1-0.3% when moving from a source thickness of 100 μg/cm^2 to 200 μg/cm^2. If only a determination of the fragment mass is persued, a 200 μg/cm^2 source thickness can be used because of its higher count rate.

5.2.2 Source Diameter

If the position of the fission fragment's origin in the source is unknown, then the larger the radial distance from the fragment's origin to the dead center of the source, the larger the uncertainty in the fragment's flight path. Increasing the source diameter thus should degrade the mass resolution, as seen with the SSB detector in Section 5.1. However, if the position of the fragment's origin in the source is known, it does not affect the uncertainty in the fragment's flight path.

The approximate position on the source that the fission fragment originated from can be determined with a DSSSD by assuming a 180^o folding angle between fragments and connecting the final positions of the fragment pair. Because the position of the fragments origin is fairly well known, the mass resolution of the DAS is not affected by changing the source diameter. The largest usable source diameter (matched to the beam diameter) would therefore be ideal to provide the highest count rate.

5.2.3 Foil Thickness and Arm Length

Since it has been determined that source thickness and source diameter have no significant effect on the mass resolution, Configuration A is now exactly the same as Configuration B and there are only two variables that can change. The effect of changing arm length on the mass resolution for a 10 μg/cm^2 foil thickness, and 100 ps timing resolution can be seen in Figure 5.5 (now including the silicon detector energy resolution).

Changing the arm length has the greatest effect on the mass resolution when the mass is smaller. At the upper end of the mass spectrum, changing the arm length has very little effect on the mass resolution. This is due to the mass resolution becoming totally dominated by the energy resolution of the silicon detector for larger mass. For A = 84, changing the arm length from 20 to 50 cm improves the mass resolution by 50%. However for A = 168, the same change in arm length leads to an

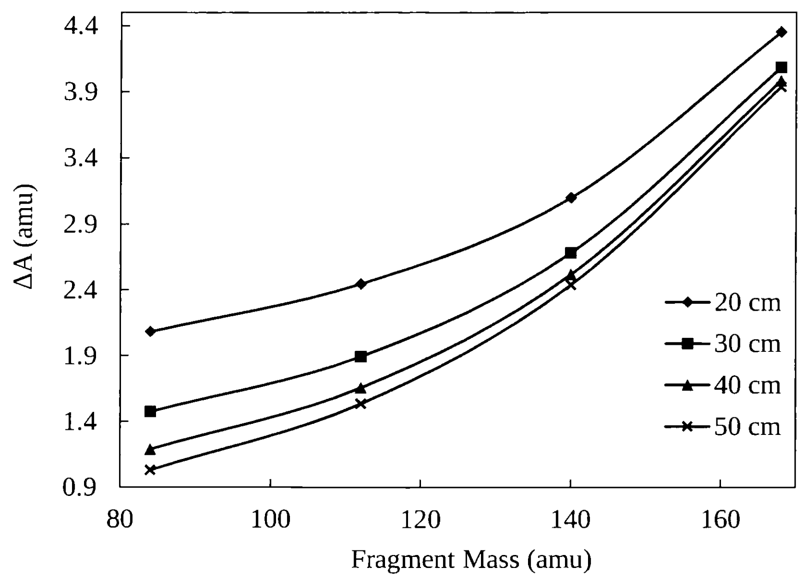

Figure 5.5: Mass resolution for a 10 μg/cm^2 foil thickness with 100 ps timing resolution.

improvement in mass resolution of only 8%. This effect is made even more apparent when looking at the percentage error for changing arm lengths, seen in Figure 5.6,

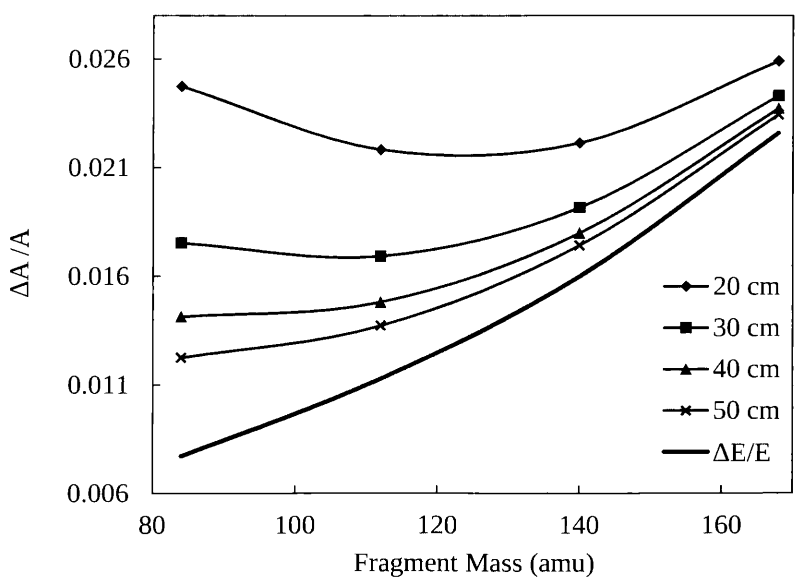

Figure 5.6: Percentage error for a 10 μg/cm^2 foil thickness with 100 ps timing resolution.

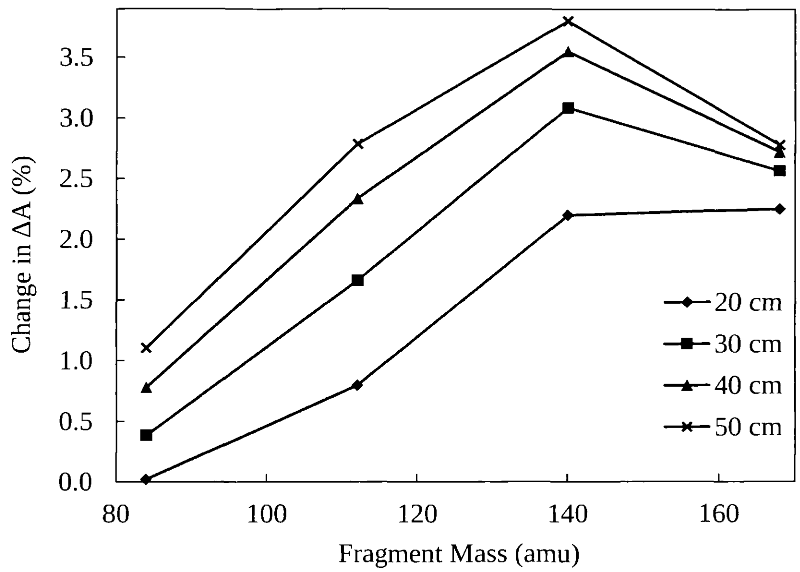

Figure 5.7: Percentage improvement in mass resolution resulting from decreasing the foil thickness from 30 μg/cm^2 to 10 μg/cm^2 with 100 ps timing resolution.

where the contribution to the mass resolution from the energy resolution of the silicon detector is plotted with the results.

The percentage improvement in mass resolution resulting from decreasing the foil thickness from 30 μg/cm^2 to 10 μg/cm^2 with 100 ps timing resolution is seen in Figure 5.7. At most, decreasing the foil thickness from 30 μg/cm^2 to 10 μg/cm^2 results in less than 4% improvement in the mass resolution with 100 ps timing resolution. The effects of changing the arm length can be neglected, and the 20 cm arm length should be used because it provides the largest solid angle.

The effect of changing arm length on the mass resolution for a 10 μg/cm^2 foil thickness, and 200 ps timing resolution can be seen in Figure 5.8. As the timing resolution degrades, the effect on mass resolution from changing the arm length increases. For A = 168, increasing the arm length from 20 cm to 50 cm results in a 24% improvement in the mass resolution. A change of 8% resulted from this effect with a 100 ps timing resolution. For A = 84, increasing the arm length from 20 cm to 50 cm results in a 57% improvement in the mass resolution. The percentage error

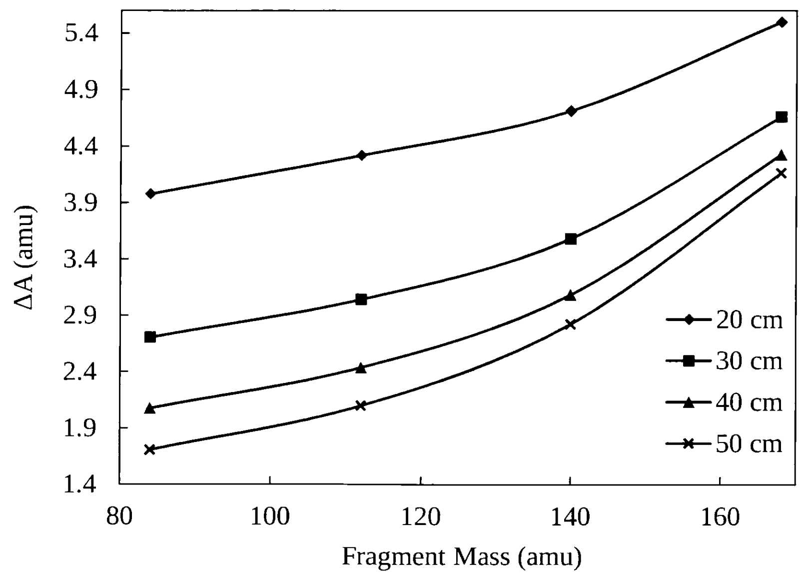

Figure 5.8: Mass resolution for a 10 μg/cm^2 foil thickness with 200 ps timing resolution.

for changing arm lengths with a 10 μg/cm^2, and 200 ps timing resolution is seen in Figure 5.9.

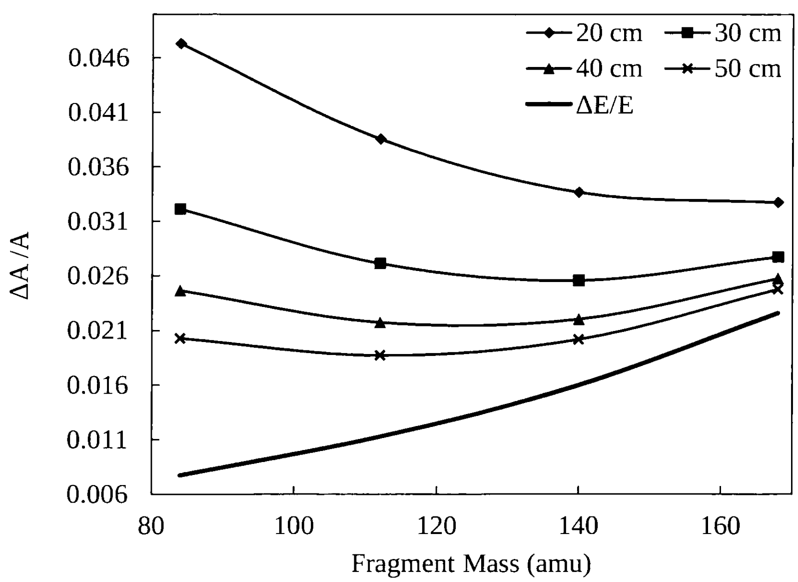

Figure 5.9: Percentage error in mass resolution for a 10 μg/cm^2 foil thickness with 200 ps timing resolution.

For a timing resolution of 200 ps, changes in arm length have a large enough effect on the mass resolution to possibly consider compromising on solid angle and extending the arm length of the DAS. Also, the mass resolution does not dominate all sources of error at higher masses like it did with a 100 ps timing resolution. Changing the timing resolution from 100 ps to 200 ps amplifies the effects of changes in arm length on the mass resolution.

For a timing resolution of 200 ps, decreasing the foil thickness from 30 μg/cm^2 to 10μg/cm^2 results in less than a 1% improvement in the mass resolution. Using a 200 ps timing resolution dominates the effects of changing foil thickness on mass resolution.

5.3 Conclusion

This work shows that the most dominant contribution to the mass resolution comes from the energy resolution of the silicon detector. Therefore, to achieve the best possible mass resolution, it is recommended that gas ionization chambers be used in the final design(56,57). In order to use a shorter arm length with the largest diameter targets possible (maximizing solid angle and count rate), it has also been shown that it is necessary to have position sensitivity of the silicon detector. When using a gas filled ionization chamber no spatial information is obtained, so position information must be obtained from the MCPs. With position sensitivity, the source diameter has no effect on mass resolution. For the purpose of mass identification, it is possible to use as thick of a fission source as desired, because energy straggling before the fragment is detected by the first MCP is irrelevant. For measurements of the total kinetic energy of a fission event, the thinnest source will be ideal in order to minimize the energy loss by the fragment in the source.

The second largest contributor to mass resolution is the timing resolution. The theoretical useful limit of timing resolution for the electrostatic mirror was found to be around 100 ps. This technical resolution cannot be fully achieved due to the limitations from the carbon foil thickness. The smallest timing resolution is predicted for the 10 μg/cm^2 foil in our simulation. If the instrumentation used can only realize a timing resolution of 200 ps, then shortening the arm length adds a significant contribution to the mass resolution. From these results, the suggested design of the DAS should have a 20 cm arm length, allows a 20 mm diameter source with a thickness on the order of 200 μg/cm^2, and a 10μg/cm^2 foil thickness.

5.4 Future Work

The next step would be to modify the simulation's fission generator to more accurately model the fission process, including neutron and gamma ray production. The undersampling and oversampling that occurs using the random generator can be eliminated with the inclusion of neutron production. If silicon detectors are used, secondary electron pickup from the silicon detector could eliminate the second carbon foil and its correction factor and associated uncertainty. Eliminating the correction factor is desired because it greatly reduces the amount of post processing needed to perform on experimental data.

Fission fragments cause strong degradation of silicon detectors due to radiation damage. The energy resolution of the detector therefore degrades over time, depending on the activity of the source. A gas ionization chamber will provide improved energy resolution over silicon detectors and will not suffer the same radiation damage, making it a more appropriate selection for detecting the energy of the fragments. In the future, the simulation should incorporate gas ionization chambers to determine what kind of energy and charge resolution can be achieved. However, the use of an ionization chamber requires the position sensitivity to come from the MCPs. Alternatively, the electrostatic energy analyzer (EEA) does not suffer the same limitations in energy resolution as the SSBD[58], and therefore may offer the potential to improve the mass resolution of the DAS. An EEA, however, usually provides a very limited solid angle coverage.

In 1997, Ter-Akopian *et al.*[59] developed a new method for investigation of low-energy and spontaneous nuclear fission, by detecting multiple gamma quanta emitted from two simultaneously produced fragments. This method was used to study spontaneous fission of ^{252}Cf, to determine yields of fission fragment pairs. The results of their work were in good agreement with experimental values for yields of fission fragment pairs. Integration of the DAS into a gamma array (e.g.[60,61] to detect both prompt and delayed emission is is planned in the future, as well as angular distribution measurements and delayed neutron detection.

REFERENCES CITED

[1] Derek L. Livesey. *Atomic and Nuclear Physics.* Blaisdale Publishing Company, 1966.

[2] Carlos A. Bertulani. *Nuclear Physics in a Nutshell.* Princeton University Press, 2007.

[3] Pierre Marmier and Eric Sheldon. *Physics of nuclei and particles*, volume 2. Academic Press, Inc., 1970.

[4] John R. Lamarsh and Anthony J. Baratta. *Introduction to Nuclear Engineering.* Prentice Hall, 2001.

[5] V.M. Strutinsky. Shell effects in nuclear masses and deformation energies. *Nucl. Phys. A*, 95:420–442, 1966.

[6] V.M. Strutinsky. "Shells" in deformed nuclei. *Nucl. Phys. A*, 122:1–33, 1968.

[7] Kenneth S. Krane. *Introductory Nuclear Physics.* John Wiley & Sons, Inc., 1988.

[8] J. Randrup and R. Vogt. Calculation of fission observables through event-by-event simulation. *Phys. Rev. C*, 80(024601), 2009.

[9] U. Brosa and S. Grossmann. In the exit channel of nuclear fission. *Z. Phys.*, 310:177–187, 1983.

[10] J. van Aarle et al. ^{252}Cf: neutron multiplicities in correlation with fission-fragment mass energy. *Nucl. Phys. A*, 578:77–92, 1994.

[11] G. Vladuca et al. Fission cross-section evaluations in the frame of the multi-modal fission model for ^{237}np(n,f). *Nucl. Phys. A*, 707:32–46, 2002.

[12] S. Oberstedt et al. Fission-mode calculations for ^{239}U, a revision of the multi-modal random neck-rupture model. *Nucl. Phys. A*, 644:289–305, 1998.

[13] Y.Z. Qian. Neutrino-induced fission and r-process nucleosynthesis. *Astrophys.*, **569**(2):L103–L106, 2002.

[14] D.G. Madland and R.J. Nix. New calculation of prompt fission neutron spectra and average prompt neutron multiplicities. *Nucl. Sci. Eng.*, 81:213–271, 1982.

[15] M. Sin et al. Fission of light actinides: ^{232}Th(n,f) ^{231}Pa(n,f) reactions. *Phys. Rev. C*, 74(014608), 2006.

[16] *Report of the Nuclear Physics and Related Computational Sciences R&D for Advanced Fuel Cycles Workshop*, 2006.

[17] U.S. Department of Energy. DOE Fundamentals Handbook Nuclear Physics and Reactor Theory DOE-HDBK-1019/2-93. Technical report, Washington, D.C. 20585, January 1993.

[18] S. Lemaire et al. Monte carlo approach to sequential neutron emission from fission fragments. *Phys. Rev. C*, 72(024601), 2005.

[19] S. Agostinelli et al. Geant4 - A Simulation Toolkit. *Nucl. Instr. Meth. A*, 506: 250–303, 2003.

[20] H. Henschel et al. Absolute measurement of velocities, masses and energies of fission fragments from Californium-252 (SF). *Nucl. Instr. Meth.*, 190:125–134, 1981.

[21] R.W. Lide H.W. Schmitt and F. Pleasonton. Indirect Measurement of Neutron Emission from Fission Fragments. *Nucl. Instr. and Meth.*, 63:237–246, 1968.

[22] H. W. Schmitt, W. E. Kiker, and C. W. Williams. Precision Measurements of Correlated Energies and Velocities of ^{252}Cf Fission Fragments. *Phys. Rev.*, 137 (4B):B837–B847, Feb 1965. doi: 10.1103/PhysRev.137.B837.

[23] H.W. Schmitt et al. Fragment energy correlation measurements for ^{252}Cf spontaneous fission and ^{235}U thermal-neutron fission. *Phys. Rev.*, 141(3): 1146–1160, 1966.

[24] S.B. Kaufman et al. A calibration procedure for the response of silicon surface-barrier detectors to heavy ions. *Nucl. Intsr. Meth.*, 115:47–55, 1974.

[25] R. Schmidt and H. Henschel. Comparison of the spontaneous fission of ^{244}Cm and ^{252}Cf. *Nucl. Phys. A*, 395:15–28, 1983.

[26] C. Budtz-Jorgensen and H.H. Knitter. Simultaneous investigation of fission fragments and neutrons in ^{252}Cf (SF). *Nucl. Phys. A*, 490:307–328, 1988.

[27] F. Busch et al. A position-sensitive transmission time detector. *Nucl. Instr. Meth.*, 171:71–74, 1980.

[28] R.D. Heil et al. A compact time-of-flight spectrometer for electrofission studies. *Nucl. Instr. Meth. A*, 239:545–550, 1985.

[29] S. Della et al. A ^{252}Cf Time-of-flight mass spectrometer with improved mass resolution. *International Journal of Mass Spectrometry and Ion Processes*, 61: 21–29, 1984.

[30] E.A. Bakkum et al. A detection system for the identification of heavy residues. *Nucl. Instr. and Meth. A*, 243:435–444, 1986.

[31] K.Th. Brinkmann et al. Comparison of different methods for the determination of fission fragment velocity, mass, and energy distributions for ^{232}Th(n,f). *Nucl. Instr. Meth. A*, 276:557–567, 1988.

[32] H.J. Whitlow et al. Mass resolution of recoil fragment detector telescopes for 0.05-0.5 A MeV heavy recoiling fragments. *Nucl. Instr. Meth. A*, 310:636–648, 1991.

[33] E. Weissenberger et al. Energy calibration of surface barrier detectors for fission fragments. *Nucl. Instr. Meth. A*, 248:506–515, 1986.

[34] Y. Zhang and H.J. Whitlow. Response of Si p-i-n diode and Au/n Si surface barrier detector to heavy ions. *Nucl. Instr. Meth. B*, 190:383–386, 2002.

[35] W.H. Trzaska et al. New approach to energy loss measurements. *Nucl. Instr. Meth. B*, 195:147–165, 2002.

[36] G.N. Knyazheva et al. Energy losses of ^{252}Cf fission fragments in thin foils. *Nucl. Instr. Meth. B*, 248:7–15, 2006.

[37] D. Comedi and J. Davies. Pulse height response of Si surface barrier detectors to 5-70 MeV heavy ions. *Nucl. Instr. and Meth. B*, 67:93–97, 1992.

[38] A.V. Kuznetsov et al. A compact Ultra-High Vacuum (UHV) compatible instrument for time of flight-energy measurements of slow heavy reaction products. *Nucl. Instr. Meth. A*, 452:525–532, 2000.

[39] S.C. Gujrathi et al. The detection of heavy ions with PIN diodes. *Nucl. Instr. and Meth. B*, 45:260–264, 1990.

[40] R. Bass et al. Design study of a magnetically focused time-of-flight spectrometer for heavy ions. *Nucl. Instr. Meth.*, 130:125–133, 1975.

[41] M. Hult et al. Empirical characterization of mass distribution broadening in ToF-E recoil spectrometry. *Nucl. Instr. and Meth. B*, 101:263–266, 1995.

[42] G.N. Knyazheva et al. Energy loss of ^{252}Cf fission fragments in thin foils. *Nucl. Instr. and Meth. B*, 248:7–15, 2006.

[43] G. Yener et al. Ranges and kinetic energies of fragments from spontaneous fission of ^{252}Cf. *Nucl. Phys. A*, 307:173–188, 1978.

[44] J.L. Wiza. Microchannel plate detectors. *Nucl. Instr. and Meth.*, 162:587–601, 1979.

[45] Glenn F. Knoll. *Radiation Detection and Measurement.* John Wiley & Sons, Inc., third edition, 2000.

[46] P.F. Hinrichsen et al. Heavy-ion resolution of SSB detectors. *Nucl. Instr. and Meth. B*, 45:275–280, 1990.

[47] et al. S. Takeda. Double-sided silicon strip detector for x-ray imaging. Technical report, SPIE Newsroom, 2008.

[48] T. Haninger et al. Folding angle and excitation energy of fragments from ^{235}U(n$_{th}$,f) and ^{252}Cf(sf) reactions. *Nucl. Phys. A*, 572:294–316, 1994.

[49] M. Kellett R. Mills H. Henriksson A. Koning, R. Forrest and Y. Rugama. *The JEFF-3.1 Nuclear Data Library.* OECD Publishing, Paris, France, 2006. JEFF Report 21.

[50] Donald E. Knuth. *The art of computer programming*, volume 2. Addison-Wesley, third edition, 1998.

[51] H. Henschel et al. Absolute measurements of velocities, masses, and energies of fission fragments from Californium-252 (SF). *Nucl. Instr. Meth.*, 190:125–134, 1981.

[52] R. Brun and F. Rademakers. ROOT - An Object Oriented Data Analysis Framework. *Nucl. Instr. Meth. in Phys. Res. A*, Sep. .

[53] D.C. Baird. *An introduction to measurement theory and experiment design.* Prentice-Hall, Inc., third edition, 1995.

[54] Wolfram Research Inc. *Mathematica.* Wolfram Research, Inc., Champaign, Illinois, version 7.0 edition, 2008.

[55] J.P. Biersack J.F. Ziegler and U. Littmark, editors. *The Stopping and Range of Ions in Solids.* Pergamon Press, New York, 1985.

[56] W.F.W. Schneider et al. Properties of a time-of-flight telescope for heavy ions in the A=100 range. *Nucl. Instr. and Meth. A*, 123:93–98, 1975.

[57] Z. Milosevich et al. Determination of nuclear charge resolution of thin film detector using a ^{252}Cf fission fragment source. *Nucl. Instr. and Meth. A*, 321: 254–258, 1992.

[58] D.J. O'Connor and T. Chunyu. Application of heavy ions to high depth resolution RBS. *Nucl. Instr. and Meth. B*, 36:178–188, 1988.

[59] G.M. Ter-Akopian et al. Yields of fragment pairs and other characteristics of spontaneous ^{252}Cf fission. *Bulletin of the Russian Academy of Sciences*, 61(4): 587–591, 1997.

[60] I. Ahmad et al. Quantitative determination of ^{252}Cf. *Nucl. Instr. and Meth. A*, 505:389–392, 2003.

[61] R.J. Gehrke et al. The γ-ray spectrum of ^{252}Cf and the information contained within it. *Nucl. Instr. and Meth. B*, 213:10–21, 2004.

APPENDIX - CONTENTS OF THE CD-ROM

The source code for the Dual Arm Spectrometer simulation along with the make file to compile the program can be found on the attached CD-ROM. The program was compiled using version 4.9.2 of Geant and data analysis was performed with version 5.22 of ROOT. The file DualArmSpectrometer.cc contains the *main* function which determines the run order for the simulation. The "/include" directory contains the class headers and the "/src" directory contains the class definitions. Note that the CD-ROM was included with this thesis for experienced Geant4/ROOT users.